DØ Note: 3376
August 25, 1998.
Draft Version 2.0

Search for Anomalous Gauge Couplings in WW/WZ $\rightarrow \mu\nu$jj: Analysis Summary

Krishnaswamy Gounder and John Ellison
University of California, Riverside, CA 92521
and
H. Thomas Diehl
Fermi National Accelerator Laboratory, Batavia, IL 60510

Abstract

We present a summary of a search for anomalous trilinear gauge boson couplings in the channel $p\overline{p} \rightarrow WW/WZ \rightarrow \mu\nu jj + X$ using Run 1B data. The observed $p_T(W)$ spectrum is characteristic of that expected from the backgrounds plus the Standard Model signal. Comparing the $p_T(W)$ spectrum to the prediction from WW/WZ production with anomalous couplings yields limits $-0.62 \geq \Delta\kappa \geq 0.78$ (for $\lambda = 0$) and $-0.45 \geq \lambda \geq 0.46$ (for $\Delta\kappa = 0$) at the 95% confidence level assuming equal WWZ and $WW\gamma$ couplings.

1 Introduction

The effective Lagrangian (CP conserving) for the description of the anomalous gauge couplings (AC) can be written as [1]:

$$i\mathcal{L}_{eff}^{WWV} = g_{WWV}\{g_1^V(W_{\mu\nu}^\dagger W^\mu - W^{\dagger\mu}W_{\mu\nu})V^\nu + \kappa_V W_\nu^\dagger W_\nu V^{\mu\nu} +$$
$$(\lambda/m_W^2)W_{\rho\mu}^\dagger W_\nu^\mu V^{\nu\rho} + ig_5^V\epsilon_{\mu\nu\rho\sigma}[(\partial^\rho W^{\dagger\mu})W^\nu - W^{\dagger\mu}(\partial^\rho W^\nu)]V^\sigma\} \quad (1)$$

where $V = Z, \gamma$. The tree level Feynman diagrams for the above process are shown in Figure 1. If CP violating terms are allowed, three more additional coupling terms will appear in the effective Lagrangian in equation (1) [2].

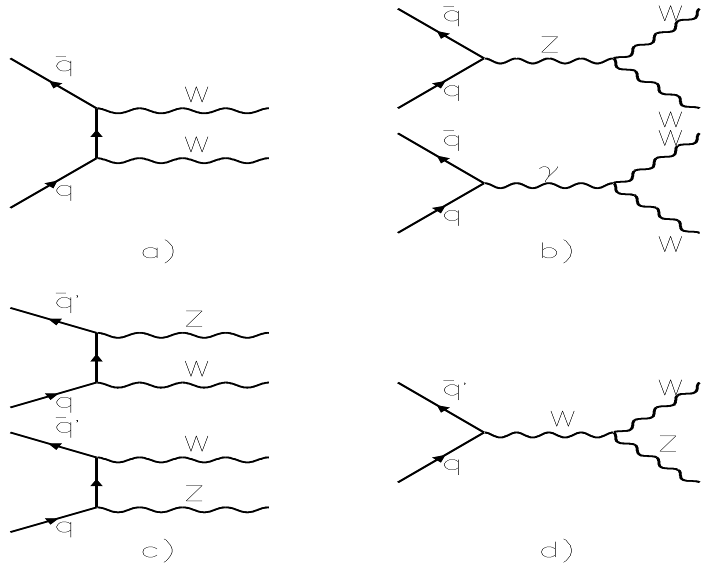

Figure 1: Diagrams for WW/WWZ production at the leading order

The overall couplings are well defined as $g_{WW\gamma}$ = e and g_{WWZ} = e cotθ_W. At the tree level Standard Model (SM), the parameters are uniquely determined: $g_1^Z = g_1^\gamma = \kappa_Z = \kappa_\gamma = 1, \lambda_Z = \lambda_\gamma = g_5^Z = g_5^\gamma = 0$. For on-shell photons, $g_1^\gamma = 1$ and $g_5^\gamma = 0$ are fixed by electromagnetic gauge invariance while g_1^Z and g_5^Z may, however, differ from their SM values. The deviations from tree level SM values can be cast as:

$$\Delta g_1^Z = (g_1^Z - 1), \Delta\kappa_\gamma = (\kappa_\gamma - 1), \Delta\kappa_Z = (\kappa_Z - 1), \lambda_\gamma, \lambda_Z, g_5^Z$$

Most theoretical arguments suggest that these anomalous couplings are significant at $O(m_W^2/\Lambda_{FF}^2)$ where Λ_{FF} is the scale of new physics. Also the limit obtained by the hadron colliders should be a function of Λ_{FF} to avoid unitary violations. For simplicity, we assume that $WW\gamma$ ($WZ\gamma$) and WWZ (WZZ) couplings are equal and study the anomalous gauge couplings for non vanishing values of the two parameters λ_V and $\Delta\kappa_V$.

The evidence for non SM physics contributions will be an enhancement in the high $p_T(W)$ region [2]. The Figure 2 illustrates the predicted number of events (for Run 1B) vs the $p_T(W)$ as a comparison for SM and non SM physics (for a set of values of λ and $\Delta\kappa$) in the muon channel. Therefore, a study of the $p_T(W)$ spectrum of WW production will provide a sensitive test of the WWZ and $WW\gamma$ couplings. A similar argument applies in the case of WZ production also. In this work, we do not distinguish between the process $W \to jj$ and $Z \to jj$ during the event selection process due to limited mass resolution of the DØ spectrometer.

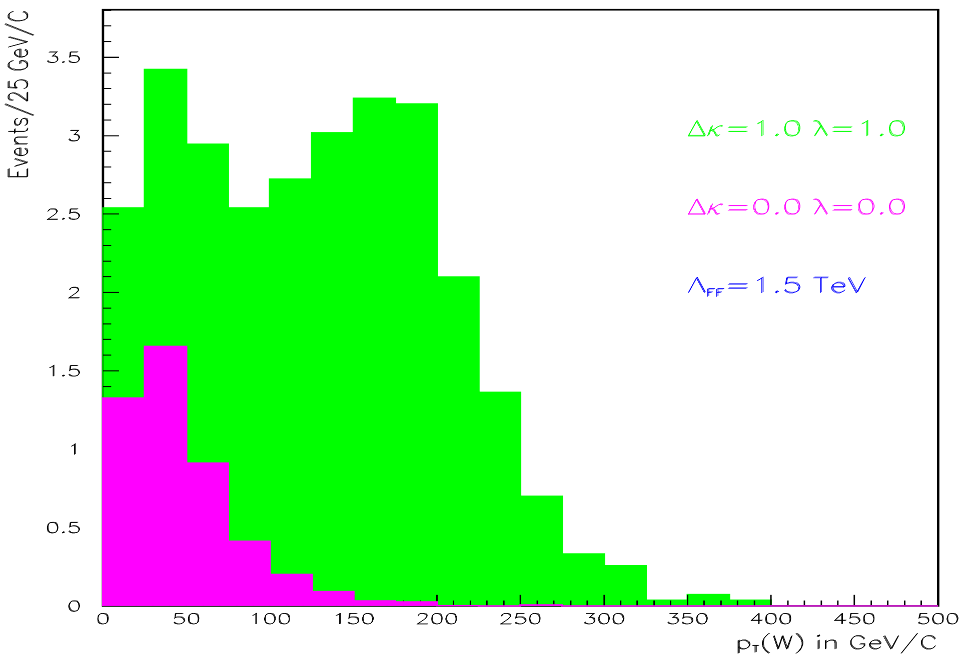

Figure 2: The comparison of $p_T(W)$ distributions predicted by the Standard Model and Anomalous Gauge Coupling for $\Lambda_{FF} = 1.5$ TeV for channel $WW/WZ \to \mu\nu jj$.

2 Event Selection

The data sample used for this work comes from Run 1B with a luminosity of 80.7 ± 4.4 pb^{-1}. During the selection process, we do not differentiate between $W \to jj$ and $Z \to jj$ decays due to the limited mass resolution of the DØ spectrometer.

2.1 Data Samples

We use three different event samples to carry out this analysis work: (a) Candidate sample from which the final data sample is selected; (b) Background data sample used for estimating the QCD multi-jet background contributions; (c) Monte Carlo event sample for computing the background contributions of W + $\geq$ 2 jets.

2.1.1 Candidate Sample

The candidate sample is the standard top group ntuple prj$root320:[top_5.ntuples. current]run1b_mjsig.rzhist. This ntuple sample of 17526 events was produced with Cafix 5.0 and a number of basic requirements including at least one jet with $|\eta| < 2.5$ and an isolated central muon with $p_T > 20$ GeV/c. The streaming selection requirements for the muon ID was the logical "or" of the two lists in Table 1. The first set is a minimal muon selection and the second set recovers muons lost due to a wrong vertex choice [3].

Streaming Cuts #1	Streaming Cuts #2
$p_T^\mu > 20$ GeV/c	$p_T^\mu < 15$ GeV/c and $p_T'^\mu > 20$ GeV/c
IFW4 ≤ 1	IFW4 ≤ 1
IQUAD ≤ 1	IQUAD ≤ 1
Cal_Confirm = .true.	$\chi^2 > 10$ or no track match

Table 1: The muon part of the data streaming requirements. $p_T'^\mu$ is the p_T given a better choice of the event vertex. "Cal Confirm" is the "or" of the following: the energy deposited in the NN (nearest neighbour) cells around the muon is greater than 0.5 GeV; there is a matching central track; HFRAC > 0.6; or Etrack > 0.5 GeV.

2.1.2 Control Data Background Sample

This sample is the data ntuple prj$root320:[top_5.ntuples.current] run1b-mjbkg.rzhist and is used for estimating the QCD multi-jet background contributions. Unlike the candidate sample, this sample does not have a cut on the muon isolation variable δR or the muon corrected missing transverse energy variable $\not\!\!E_T$.

2.1.3 Monte Carlo Background Sample

This sample prj$root320:[top_5.ntuples.new]W2L80AJHW-Z.rzhist is used to estimate the background contributions of W + $\geq$ 2 jets. This was generated with the program VECBOS followed by HERWIG to hadronize partons and D0GEANT for the detailed simulation of the detector. This corresponds to a luminosity of 69.8 pb^{-1} [4].

2.2 Global Event Selection and Trigger

For any event to be considered for selection, it should have a primary interaction vertex and not be associated with the Main Ring beam conditions (Micro Blank or MRBS or the calorimeter recovery time). Each event should be also selected by the μ-jet trigger listed below.

Table 3 lists the characteristics of the μ-jet triggers used in the analysis. Each has a level 1 and a level 2 component to the muon and jet parts. Here's what the arcane nomenclature means. For all of these triggers, the first number in parenthesis is the minimum number of objects of the type required. For level 1 muons, the second character string is the pseudorapidity region. $y1$ indicates the CF; $y2$ indicates the CF plus EF. For level 1 jets, the second character string is the trigger tower minimum E_T. For level 2 muons, the second and third (or more) character strings are the minimum p_T and the quality descriptors of the muon. For level 2 jets, the second and third character strings are the minimum E_T and the pseudorapidity region.

2.3 Muon Identification

We require only one muon in a given event with the following characteristics:

- Central Muons only (IQUAD $\leq$ 4)

Version	Run Range	Muon Filter	Filter Bit	Mu_jet Filter	Filter Bit
8.0	70000-72733	Mu_1_Max	5	Mu_jet_High	14
8.1	72734-73724	Mu_1_Max	5	Mu_jet_High	14
8.2	73725-74192	Mu_1_Max	5	Mu_jet_High	14
8.3	74193-75038	Mu_1_Max	5	Mu_jet_Cal	14
8.4	75039-75142	Mu_1_Max	5	Mu_jet_Cal	14
8.5	75143-76176	Mu_1_Max	5	Mu_jet_Cal	14
8.6	76177-77824	Mu_1_Max	5	Mu_jet_Cal	14
8.7	77825-79982	Mu_1_Max	5	Mu_jet_Cal	14
9.0	79983-81906	Mu_1_Max	5	Mu_jet_Cal	14
9.1	81907-83212	Mu_1_Max	5	Mu_jet_Cal	14
9.2	83213-85276	Mu_1_Max	5	Mu_jet_Cal	14
10.0	85277-86276	Mu_1_Max	4	Mu_jet_Cal	13
10.1	86277-87803	Mu_1_Max	4	Mu_jet_Cal	13
10.2	87804-89517	Mu_1_Max	5	Mu_jet_Cal	13
10.3	89518-89891	Mu_1_Cent_Max	6	Mu_jet_CenCal	14
10.4	89892-91922	Mu_1_Cent_Max	6	Mu_jet_CenCal	67
10.5	91923-92827	Mu_1_Cent_Max	6	Mu_jet_CenCal	67
10.6	92828-99999	Mu_1_Cent_Max	6	Mu_jet_CenCal	67

Table 2: List of muon triggers used for the event selection. The μ-jet triggers are unprescaled and require L1.0 muon while μ triggers are prescaled with L1.5 requirement.

- $p_T(\mu) > 20$ GeV
- Isolation from jets: δR > 0.5
- Muon quality: IFW4 ≤ 4
- Hfrac > 0.75 and Efrac_H(1) > 0.0 or HFrac $= 1.0$
- A-stubs vetoed
- IPBP < 20.0 cm and IPNBP < 20.0 cm
- $\int B.dL > 0.6$
- $T^0_{float} < 100$ ns.

Range	Trigger	Level 1	Level 2
V8.0-V8.2	Mu-Jet-High	$\mu(1, y2)$ Jet(1,5)	$\mu(1, 8, \text{good})$ Jet(1,15)
V8.3-V10.2	Mu-Jet-Cal	$\mu(1, y2)$ Jet(1,5) Jet(1,3)	$\mu(1, 10, \text{good})$ Jet(1,15, $\lvert\eta\rvert < 2.5$)
V10.2-V10.6	Mu-Jet-Cal	$\mu(1, y1)$ Jet(1,5, $\lvert\eta\rvert < 2.0$) CS	$\mu(1, 10, \text{good}, \text{cal}, \text{scint})$ Jet(1,15,$\lvert\eta\rvert < 2.5$)

Table 3: Characteristics of the level 1 and level 2 μ-jet triggers used in the analysis. The arcane nomenclature is decoded in the text.

The first item corresponds to a fiducial cut of $\eta \leq 1.0$ for the muons. The fourth item indicates reasonable quality-off-fit of the muon using information from the muon system only. The fifth item serves to reject combinatoric fakes and cosmic rays and is often refered as "MTC" cut. While the sixth item rejects muons having no B/C layer hits, the seventh and the ninth item provides further protection against cosmic and misreconstructed muons. The IPBP and IPNBP are the 2-D distances-of-closest approach between the muon and the associated primary vertex in the bend and non-bend projections respectively. The $\int B.dL$ cut insures that muons have transversed enough magnetic field to provide an acceptable p_T measurement. The $p_T(\mu)$ and δR (distance in $\eta - \phi$ space to the nearest 0.5 cone jet) requirements select the muons with characteristics of those from W decays.

2.4 Jet Selection

For this work, we use jets with fixed cone radius of 0.5 in $\eta - \phi$ space and are corrected with CAFIX V5.0. We require each event with at least two jets with the following qualifications:

- E_T(jet)$>$ 20 GeV
- $|\eta(\text{jet})| < 2.5$
- Quality: $0.1 <$ EMfrac <0.9; $-0.1 <$ CHFrac < 0.75
- 50 GeV $<$ Dijet Invariant Mass m(jj) $<$ 110 GeV

For events with more than two good (satisfying above criteria) jets, we use the jets with the highest invariant mass. The jet quality cuts (item 3) on the jet electromagnetic fraction and coarse hadronic fraction help suppress backgrounds from isolated noisy calorimeter cells and the accelerator (Main Ring) losses.

2.5 Missing $\not\!\!E_T$ and Kinematical Criteria

In this work, we use the muon corrected missing transverse energy $\not\!\!E_T$ through out. We require that each event has an $\not\!\!E_T$ of at least 20 GeV. We also apply a kinematic criteria to each event to suppress the background, $M_T > 40$ GeV where the transverse mass $M_T(\mu\nu)$ is defined as:

$$M_T(\mu\nu) = \sqrt{2.E_T^{\mu}.\not\!\!E_T.(1 - \cos(\phi_\mu - \phi_\nu))}$$

.

2.6 Luminosity

We compute the luminosity for the set of triggers shown in Table 2 using the utility GET_FILT_LUM by eliminating bad runs (~hobbs/analysis/rcp/bad_runs.rcp). Further, we correct the luminosity for the offline cuts on the Main Ring effects using the data as some events (about 15%) in the data sample tagged by the μ-jet trigger but fails the clean event requirements. The final luminosity for this study is estimated to be 80.7 pb^{-1}.

2.7 Final Data Sample

Using the above event selection cuts, we obtain the final data sample of 224 events. The final p_T distributions for $W \to \mu\nu$ and $W/Z \to jj$ are shown in Figures 3 and 4. As expected, the distributions peak at low p_T and are empty for $p_T(W) > 150$ GeV.

We have also shown the dijet invariant mass distribution m(jj) before the W/Z mass cut and the $W(\mu\nu)$ transverse mass spectrum in Figures 5 and 6 for reference.

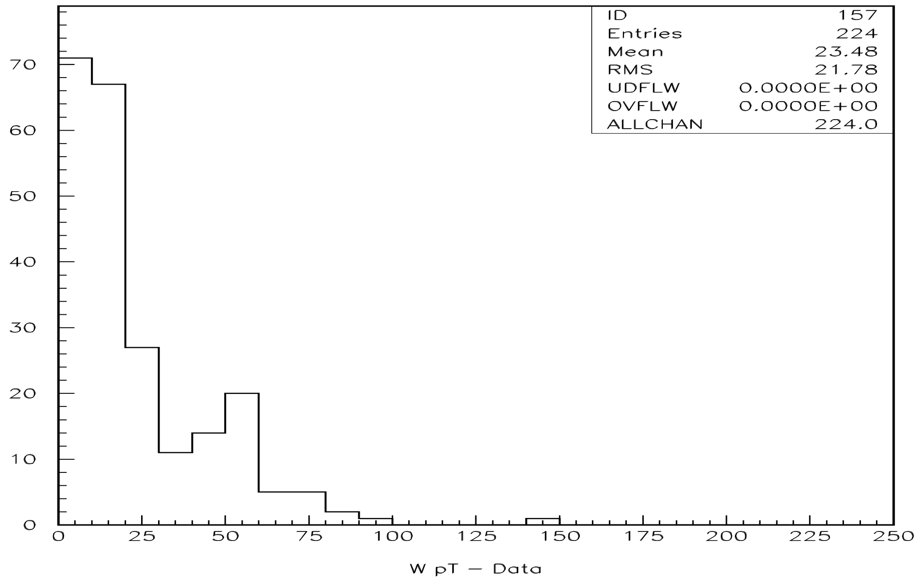

Figure 3: The $p_T(W)$ distribution for the final data sample. The distribution peaks at low p_T and empty (no event present) for $p_T(W) > 150$ GeV.

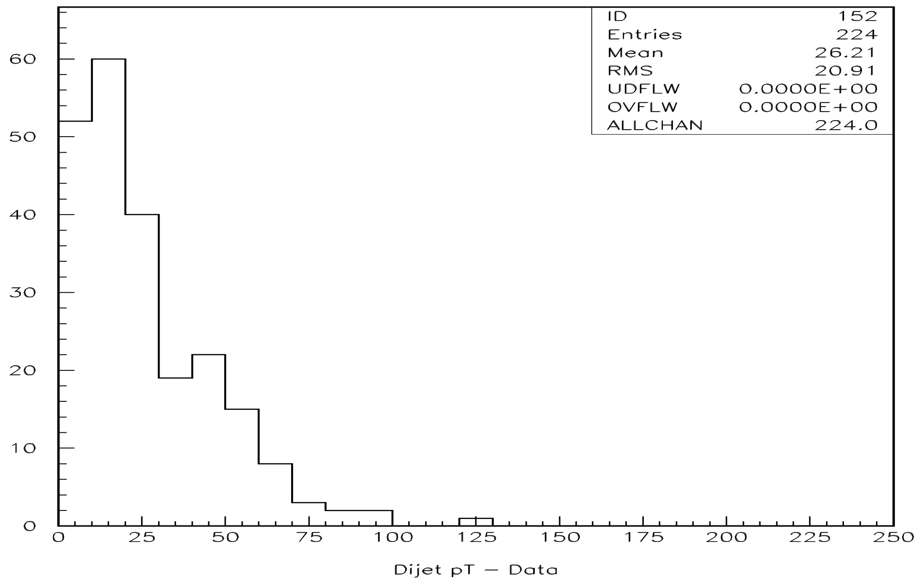

Figure 4: The $p_T(jj)$ distribution for the final data sample. As in the case of $p_T(W)$ distribution, it is empty for $p_T(jj) > 150$ GeV.

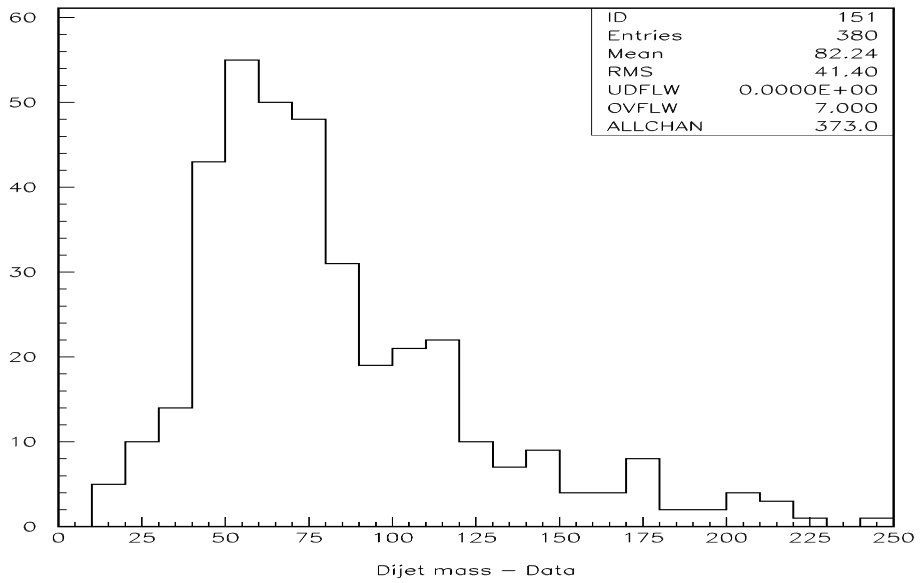

Figure 5: Dijet Mass distribution for the final data sample before the $W/Z \to jj$ mass cut: $50 < \mathrm{m(jj)} < 110$ GeV.

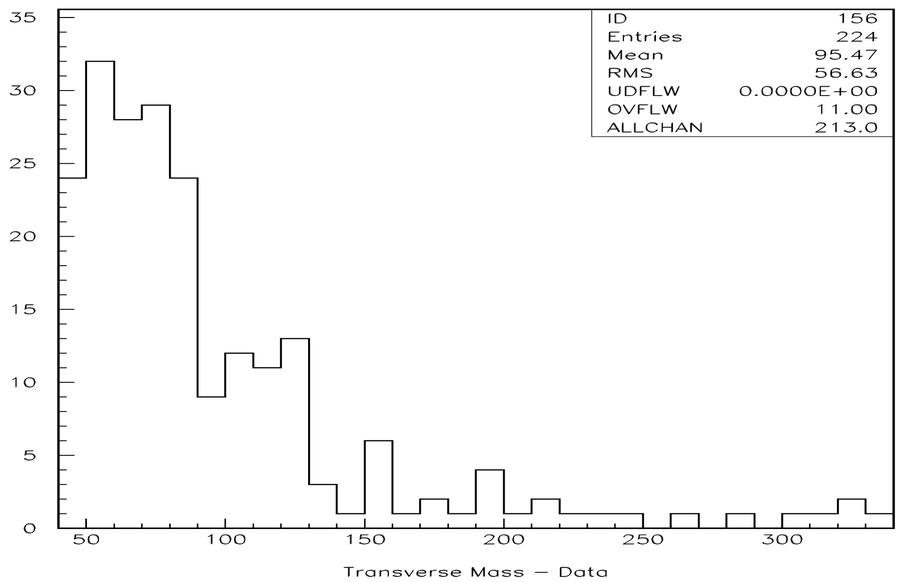

Figure 6: $W(\mu\nu)$ transverse mass distribution for the final data sample.

3 Reconstruction Efficiency

In this section we discuss the trigger efficiency, the muon and jet identification efficiencies, and their contributions to the systematic uncertainty.

3.1 Trigger Efficiency

The trigger efficiency calculation has two components. The first is from the muon part and the second from the jet part of the trigger. Recall that Table 2 lists the Mu_Jet triggers used in the event selection.

3.1.1 Jet trigger efficiency

We measured the jet component of the trigger efficiency using events with a muon and a single reconstructed jet. The muon must have been in the central region and pass the same quality criteria as the signal. The jet was also required to pass the same quality criteria as the jets in the signal sample. We used all such events which passed the muon filters listed in Table 2. As the muon components of these single muon triggers are more restrictive than the muon components of the Mu_jet triggers, an unbiased sample is provided. The efficiency is simply the fraction of events which passed the Mu_jet filters, as a function of jet E_T, binned in detector eta for three pseudorapidity regions. A three parameter fit to the data using an error function was performed. The specific formula used for the efficiency was

$$\epsilon = 0.5 * A * (1.0 + \mathrm{ERF}(X)), \tag{1}$$

where $X = C * p_T(jet) - C * B$. A is the plateau. B is E_T at which the trigger is 50% efficient. C is the steepness of the trigger turn-on. The χ^2's of the fits were typically 14 to 18 with typically 18 degrees of freedom. Table 4 summarizes the results of the fits. Figure 3.1.1(a)-(c) shows the efficiency of the data as a function of p_T as well as the fit for the three pseudorapidity regions. For SM fast Monte Carlo events which passed the rest of the selection criteria, the jet trigger efficiency was $0.927 \pm 0.007(stat)$. If we used an alternative fit, where the plateau efficiency was constrained to 1.0, the overall efficiency was 0.012 higher (1.3% fractionally); we take that as a contribution to systematic uncertainty.

Eta Range	A	B	C
$\lvert\eta\rvert < 1.0$	0.959	20.405	0.0942
$1.0 < \lvert\eta\rvert < 1.5$	0.878	27.069	0.0665
$1.5 < \lvert\eta\rvert < 2.5$	1.0	23.492	0.0922

Table 4: Parameters for the jet trigger turn-on curves vs. η region.

3.1.2 Muon trigger efficiency

The muon trigger efficiency is taken as the luminosity-weighted average of the components [5] of the L1 and L2 muon trigger criteria. These include the efficiencies of the L1 CCT, L1 scintillator, L2 "cal" cut, and L2 "good" criteria, for the applicable run ranges as indicated in Table 3. The offline $p_T(\mu)$ cut of 20 GeV/c is sufficiently high so that the L2 $p_T(\mu)$ threshold of 10 GeV/c contributes no inefficiency. The efficiency for the preshutdown sample is 0.722 ± 0.016. For the postshutdown sample, it is 0.683 ± 0.028. The weighted average, taking some uncertainties as correlated, is $\epsilon_{\mu\mathrm{trig}} = 0.707 \pm 0.018$.

3.2 Jet Identification Efficiency

The jet selection criteria has an efficiency[9, 10] of 0.96 ± 0.01 on a per jet basis. That's also what we get from the Pythia simulation. We use twice 1% for our jet ID uncertainty. Another uncertainty arises due to the effect of our lack of knowledge of the jet energy scale which effects the efficiency through the jet E_T selection and dijet mass selection. This was estimated in Ref. [11] as 3%. We performed a cross check by increasing and decreasing the jet energies by 10% in a modified version of the fast detector simulation where we implemented the jet fiducial, jet threshold, and and dijet mass selection selection criteria directly. These changes in energy scale lead to changes of the efficiency of +6.6% and -8.8%, respectively. Given that the energy scale uncertainty is closer to a third that size, we take this as confirmation of Alberto's number and use 3%. The uncertainty on the efficiency due to uncertainty in the jet resolution was investigated by applying a different set [11] of jet resolutions in the fast Monte Carlo than is described in Sec. 5. There was no difference in the efficiency between the two sets.

A bunch of jet-related efficiencies have been mentioned in this section which are accounted for in the Monte Carlo. We find it useful to summarize the uncertainties at this time. Including the uncertainty on the efficiency of the jet part of the trigger, and those uncertainties mentioned above, we have a net fractional uncertainty of 3.8%.

3.3 Muon Identification Efficiency

The muon reconstruction efficiency comes from a variety of sources including data-based measurements and Monte Carlo simulation. The efficiency for the fiducial selection criteria (MUOT) and the minimum field integral criteria comes from Monte Carlo simulation. It is implicit in the Pythia simulations discussed in Section 5 and explicitly implemented in the fast Monte Carlo simulations as discussed there as well. The component of the efficiency due to random overlap of the muon with a jet from the decay of the other W or Z is also Monte Carlo based. The total of these two components amounts to 0.28 ± 0.01 in the MC with fast detector simulation. The remainder of the components of the muon reconstruction efficiency are listed in Table 5 and are based on data. The additional 10% systematic uncertainty is assigned to the muon selection efficiency because of the difference between the ratios of muon + jet events to electron + jet events in data and Monte Carlo [6]. Overall, these efficiencies amount to $0.680^{+0.041}_{-0.080}$.

Selection Criteria	Efficiency
Muon quality: IFW4 ≤ 4	0.941 ± 0.015 [7]
Isolation from random jets	$0.916 \pm 0.016 \pm 0.042$
MTC	0.932 ± 0.017 [7]
IPBP < 20.0 cm and IPNBP < 20.0 cm	0.99 ± 0.01 [7]
$T^0_{float} < 100$ ns	0.93 ± 0.01 [7]
Dave's scanning factor	0.92 ± 0.02 [8]
Unexplained losses	$1.0^{+0.00}_{-0.10}$ [6]
Only one isolated muon	$1.00^{+0.00}_{-0.01}$
Total of these components	$0.680^{+0.041}_{-0.080}$

Table 5: Muon reconstruction efficiencies excluding the losses due to the fiducial and field integral criteria.

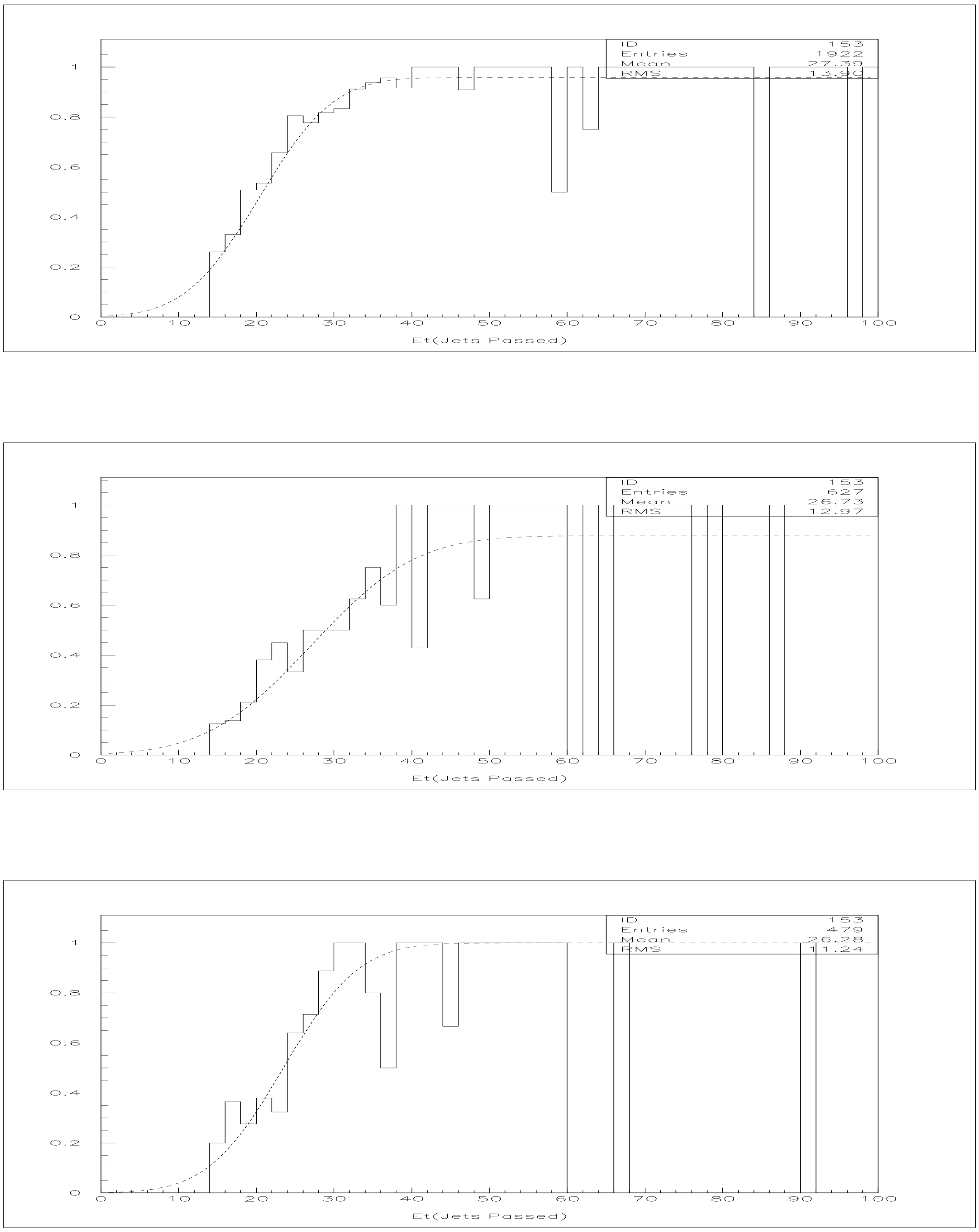

Figure 7: The efficiency as a function of $E_T(jet)$ for the jet part of the triggers used in the analysis. The upper figure is for $|\eta| < 1.0$, the middle figure is for $1.0 < |\eta| < 1.5$ and the lower figure is for $1.5 < |\eta| < 2.5$.

4 Background Estimations

There are many sources of backgrounds to the decay $WW/WZ \rightarrow \mu\nu jj$ with real (physical) as well as instrumental (fake) contributions. The physical backgrounds mainly arise from the same final state decay products while the instrumental sources are due to physical process mimicking the decay products of interest as a consequence of apparatus misidentification or mis-measurement. Below, we list possible processes contributing as backgrounds to the channel of interest.

- QCD multi-jet fakes
- W + $\geq$ 2 jets
- $t\bar{t} \rightarrow W^+W^-b\bar{b} \rightarrow \mu\nu_\mu jjX$
- $WW/WZ \rightarrow \tau\nu_\tau jj \rightarrow \mu\nu_\mu\nu_\tau jjX$
- $ZX \rightarrow \mu^+\mu^-X$
- $ZX \rightarrow \tau^+\tau^-X \rightarrow \mu\nu_\mu jjX$
- Punch-through and decays in flight
- Cosmic ray muons

Among the processes listed above, the items 1 and 2 contribute most of the backgrounds while the rest of the list only a small (neglible) amount at the final reconstructed stage after all the relevant event selection cuts.

4.1 QCD Multi-jet Background

We estimate the multi-jet background using the technique of muon fake rate developed by the Top Group [12]. In this method, the background at N jets is calculated by multiplying the number of N+1 jets non-isolated muon events satisfying all the analysis requirements by the probability that a μ+jet system appears as an isolated muon.

- A non-isolated muon is a muon which satisfies all requirements for an isolated muon except that $\delta R < 0.5$. Such events arise dominantly from $p\overline{p} \rightarrow q\overline{q} + X$ processes.

- The fake rate for N jets is the ratio of the number of isolated muon events having N jets and $\not\!\!E_T$< 20 GeV to the number of non-isolated muon events having N+1 jets and $\not\!\!E_T$< 20 GeV.

- The fake rates are computed using Run 1B events that satisifies all analysis requirements except with $\not\!\!E_T$< 20 GeV and with out the muon isolation cut of $\delta R > 0.5$.

Using the fake rates obtained using the technique explained above and the number of non-isolated N jet events satisfying the analysis cuts, we compute the multi-jet background as shown below. The sample used for this study is Run 1B background ntuple prj$root320: [top_5.ntuples.current] run1b-mjbkg.rzhist explained in section 2.

Item	M(jj): 50-110 GeV	<50; >110 GeV
Iso. μ for 1<njet<8; $\not\!\!E_T$< 20 GeV	31±5.6	17±4.1
Non-iso. μ for 2<njet≤8; $\not\!\!E_T$< 20 GeV	760±27.6	416±20.4
Muon fake rate	0.041±0.007	0.041±0.010
Non-iso. μ for 2<njet≤8; $\not\!\!E_T$> 20 GeV	2567±50.7	1339±36.6
Estimated multi-jet background	104.7±19.3	54.719±13.6

Table 6: Summary of Multi-jet background estimation. The errors shown are statistical only. The background estimation in the out of mass range is necessary for normalizing $W+\geq 2$ jets contribution.

4.2 W + $\geq$ 2 Jets

Due to large cross section for W + jets events, we may expect this to be the dominant background. Here, two jets artificially combine to mimick the decay $W/Z \rightarrow jj$ while there is an isolated muon (real or fake) happen to be present in the event. To estimate the W + $\geq$ 2 jets background, we use a Monte Carlo sample generated with the VECBOS program followed by HERWIG to hadronize the partons and D0GEANT for the detailed simulation of the detector. The corresponding ntuple is

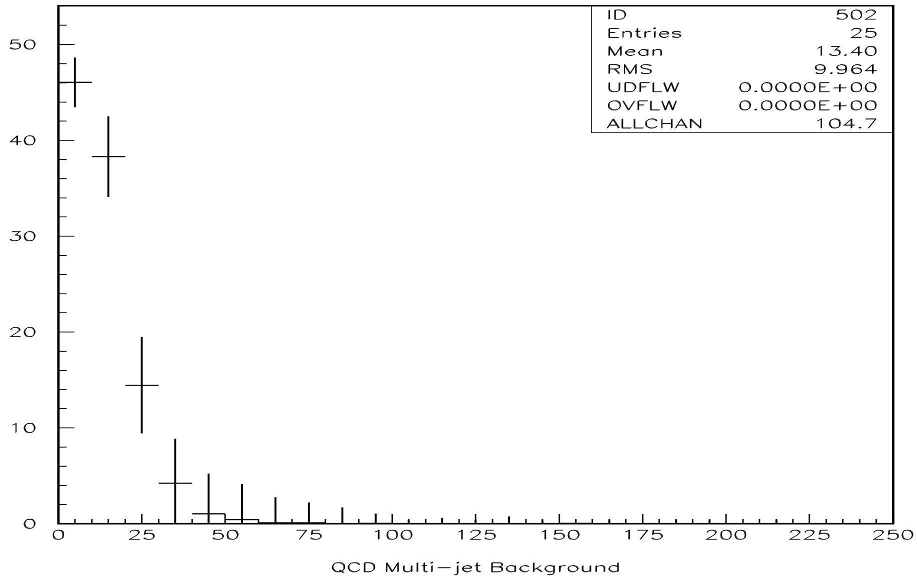

Figure 8: QCD Multi-jet background: $p_T(W)$ distribution

one of the standard Top group ntuple from the area: prj$root320: [top_5.ntuples.new] W2L80AJHW-Z.RZHIST corresponding to a luminosity of 69.8 pb^{-1}.

First, we apply the final selection cuts to the above sample and the resulting histogram is shown in Figure 9. As the cross section for W + $\geq$ 2 jets production has a large uncertainity, we normalize this to the out of mass range (0-50 GeV; 110-500 GeV) data after subtraction of the QCD Multi-jet background. The details of the normalization parameters are summarized in Table 7. The final background contribution due to the $W+\geq 2$ jets iss 117.1 $\pm$ 23.9 events. To cross check, we compute the cross section for $W+\geq 2$ jets as (28317 * 0.421)/80.7 = 137.03 pb which is in good agreement with 135 pb given by the VECBOS program. Here, the 28317 is the number of events in the Monte Carlo sample, 0.421 is the normalization factor and the 80.7 is the Run 1b integrated luminosity for the muon channel.

4.3 Contributions from Other Backgrounds

Among the backgrounds, $t\bar{t} \rightarrow W^+W^-b\bar{b} \rightarrow \mu\nu_\mu jjX$, $WW/WZ \rightarrow \tau\nu_\tau jj \rightarrow \mu\nu_\mu jjX$, $ZX \rightarrow \mu^+\mu^-X$ and $ZX \rightarrow \tau^+\tau^-X \rightarrow \mu\nu jjX$, only non negligible contribution comes from the $t\bar{t}$ decays. The background from this process is estimated below in detail.

The background muons due to hadrons punching through the calorimeter and the inflight $\pi/K \rightarrow \mu$ decays can be ignored due to the thickness of the calorimeter and the muon system. Also, the high p_T requirement ($> 20.0 GeV$) on the muons suppresses this background. The cosmic ray muon background is suppressed heavily

Type	Events
Data Events - out of mass range	155.0±12.5
Estimated Multi-jet background - out of mass range	54.7±13.6
W + $\geq$ 2 jets background - out of mass range before norm.	238.0±15.4
Normalization constant	0.421±0.082
W + $\geq$ 2 jets events in mass range before norm.	278.0±16.7
Estimated W + $\geq$ 2 jets background in the mass region	117.1±23.9

Table 7: Summary of W + > 2 jets background estimation. The errors shown are statistical only.

by the floating cut on T^0 and the requirements of $p_T(\mu)$, as well as the presence of $W/Z \to jj$ in a given event.

The process $ZX \to \mu^+\mu^-$ + jets also contributes to the background when one of the muons is missing. But then, this process resembles those from the $W+\geq 2$ jets decays and has the same kinematic characteristics. Therefore, this is actually accounted for during the $W+\geq 2$ jets normalization as explained above.

As the event selection procedure employed includes all events with number of jets greater than one, the events via the decay $t\bar{t} \to W^+W^-b\bar{b} \to \mu\nu_\mu jjX$ will contaminate the final sample. To estimate the contribution, we use the Monte Carlo ntuple sample prj$root320:[top_5.ntuples.current]LJETS170-Z.RZHIST. This sample was produced with VECBOS followed by HERWIG to hadronize the partons and D0GEANT for detector simulation with a top mass of 170 GeV/c^2. Assuming a top cross section of 5.5 ± 1.8 pb [13], we obtain 2.7 ± 1.2 (total) events for a luminosity of 80.7 pb^{-1}. The resulting $p_T(W)$ distribution is shown in Figure 11.

4.4 Final Data/Background Distributions

A comparison of the contribution of various processes for the final data sample is shown in Table 8. The errors shown are statistical only. The distributions for the major backgrounds and final data sample is shown in Figure 12. As a cross check, we have also shown the distributions for other relevant paramaters such as dijet p_T, dijet mass, muon p_T, $\not{E}_T$ and transverse mass $M_T(W)$ for the background as wellas for the final data sample in Figures 13- 17. These distributions indicate that our background estimations are quite reasonable. Moreover, when the cuts are varied from the standard cuts, the data and the background distributions are also consistent

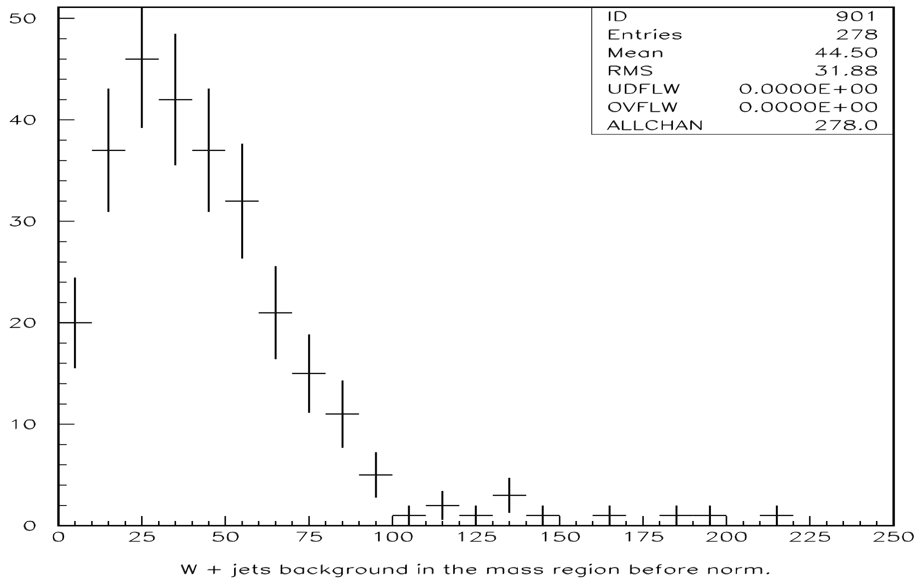

Figure 9: W + $\geq$ 2 jets before normalization: $p_T(W)$ distribution.

showing the validity of our background estimation techniques. The Figures 18, 19, 20, and 21 show the comparison of distributions for standard cuts except for p_T(j) $>$ 25 GeV/c, $M_T(\mu\nu)$ $>$ 45 GeV/c, $\not{E}_T >$ 25 GeV/c, and $p_T(\mu)$ $>$ 25 GeV/c respectively. The relevant event counts are summarized in Table 9.

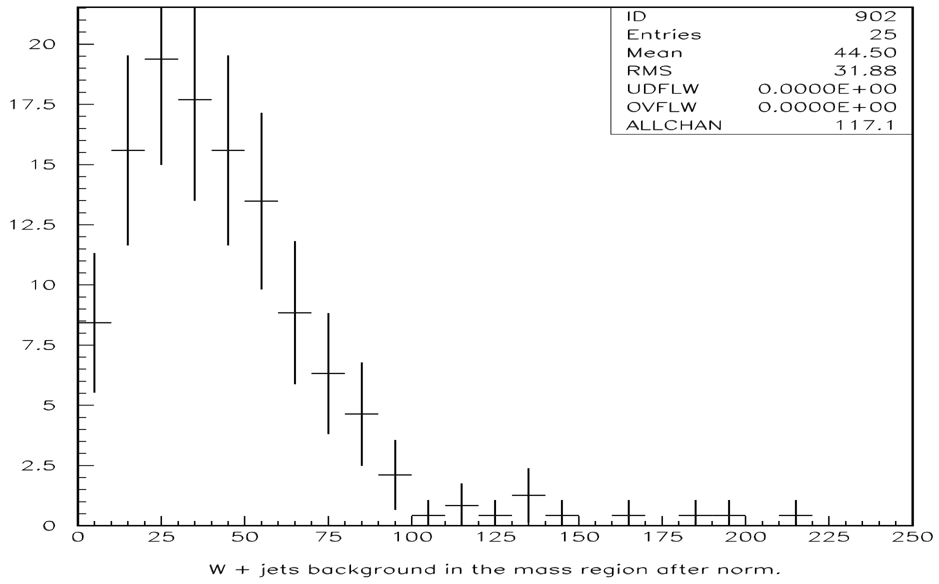

Figure 10: W + $\geq$ 2 jets after normalization: $p_T(W)$ distribution.

4.5 Background Systematics

The major factors contributing to the background systmatics are the uncertainities associated with the selection parameters such as $\not{E}_T$, muon isolation parameter δR, W transverse mass, dijet mass window along with the jet energy scale. As any change in the QCD multi-jet background estimation affects the W + $\geq$ 2 jets background contribution, we estimate the total combined background systematic uncertainity. In each case, we vary the relevant parameter by $\pm\sigma$ where σ is the relevant detector resolution and compute the resulting uncertainity for the final background contribution. The results are summarized in Table 10. In the case of jet energy scale, the resolution parameter σ is given by [14]:

$$(\sigma_E/E)^2 = (N/E)^2 + (S/\sqrt{E})^2 + C^2$$

where the parameters N, S, and C represent the noise, sampling and constant terms respectively. More details can be found elsewhere [14]. The final systematic uncertainity is obtained by adding all the relevant contributions in quadrature.

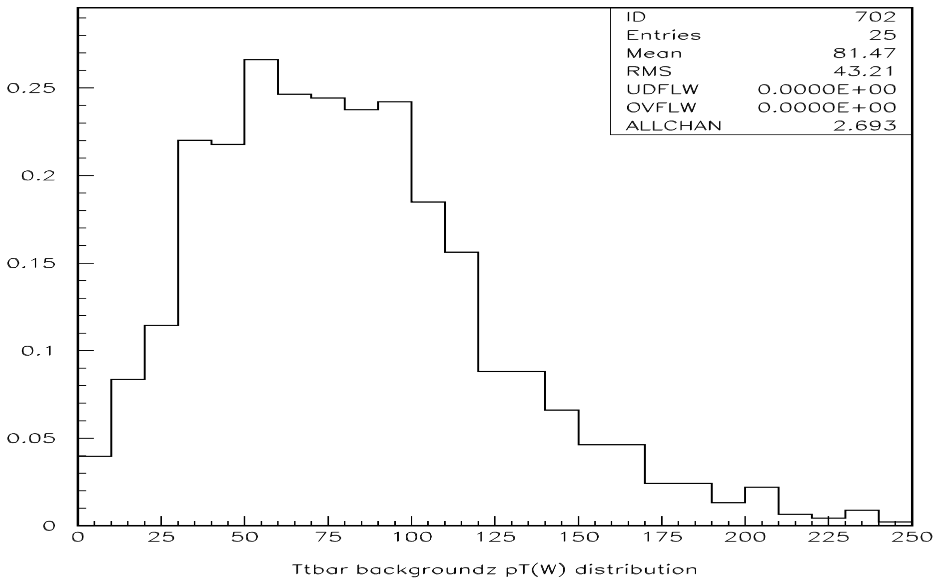

Figure 11: $t\bar{t}$ background after normalization: $p_T(W)$ distribution.

Sample	Run 1B
Luminosity	80.7 pb^{-1}
QCD Multi-jet Background	104.7±19.3
W + > 2 jets Background	117.1±23.9
Additional Backgrounds	2.7±1.2
Total Background	224.5±30.7
Final Data Sample	224.0±15.0

Table 8: Comparison of final data sample and various background contributions for $WW/WZ \to \mu\nu jj$.

Variation	QCD Multi-jet	$W + \geq$ 2 jets	Total Bkg.	Data Sample
p_T(j) > 25 GeV/c	45.9 ± 12.5	65.6 ± 20.9	111.5 ± 24.4	118.0 ± 10.9
$M_T(\mu\nu)$ > 45 GeV/c	118.5 ± 30.4	95.7 ± 29.4	214.2 ± 42.3	212.0 ± 14.6
$\not{E}_T$ > 25 GeV/c	100.0 ± 12.3	98.3 ± 19.0	198.2 ± 22.6	192.0 ± 13.9
$p_T(\mu)$ > 25 GeV/c	99.3 ± 19.0	104.0 ± 22.4	203.3 ± 29.4	199.0 ± 14.1

Table 9: Comparison of final data sample and various background contributions for $WW/WZ \to \mu\nu jj$ for variation of standard cuts.

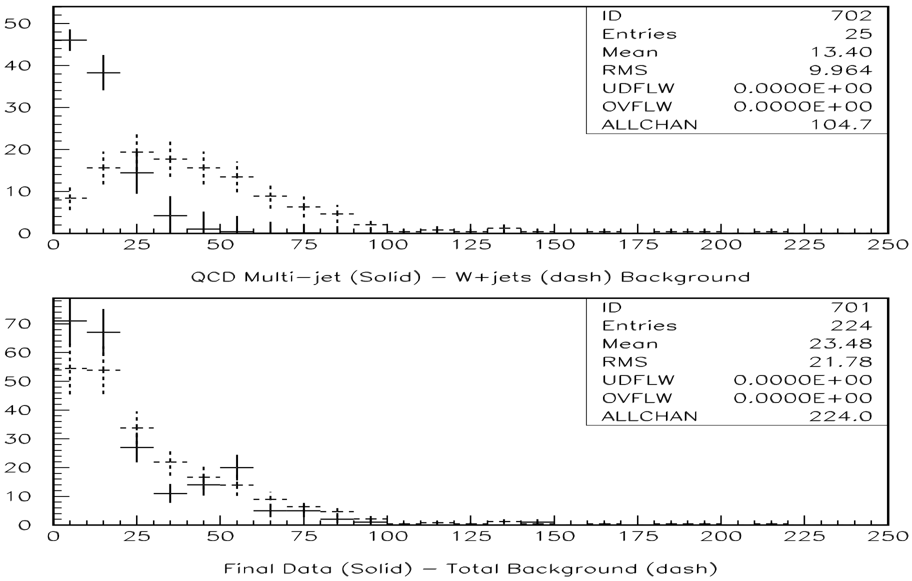

Figure 12: Comparison of data and background distributions: $p_T(\mu\nu)$

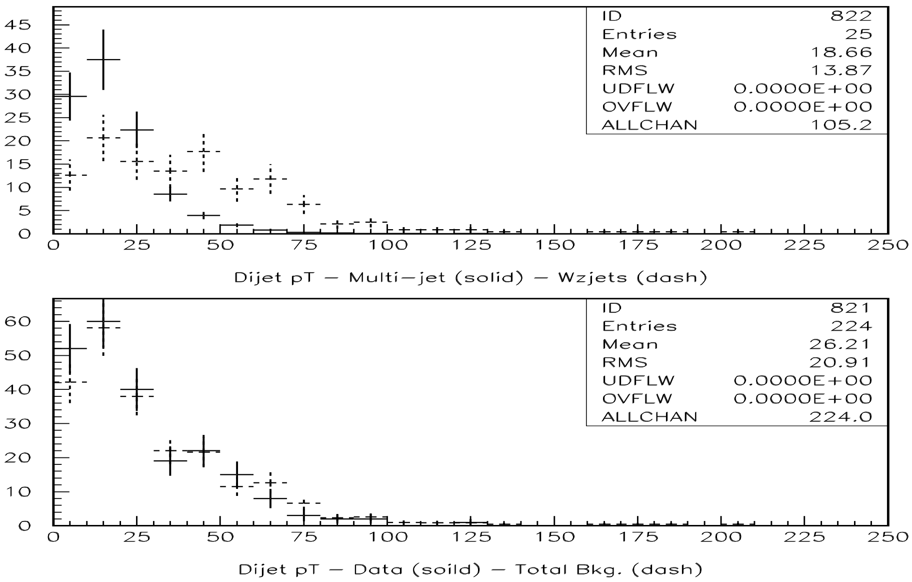

Figure 13: Comparison of data and background distributions: $p_T(jj)$

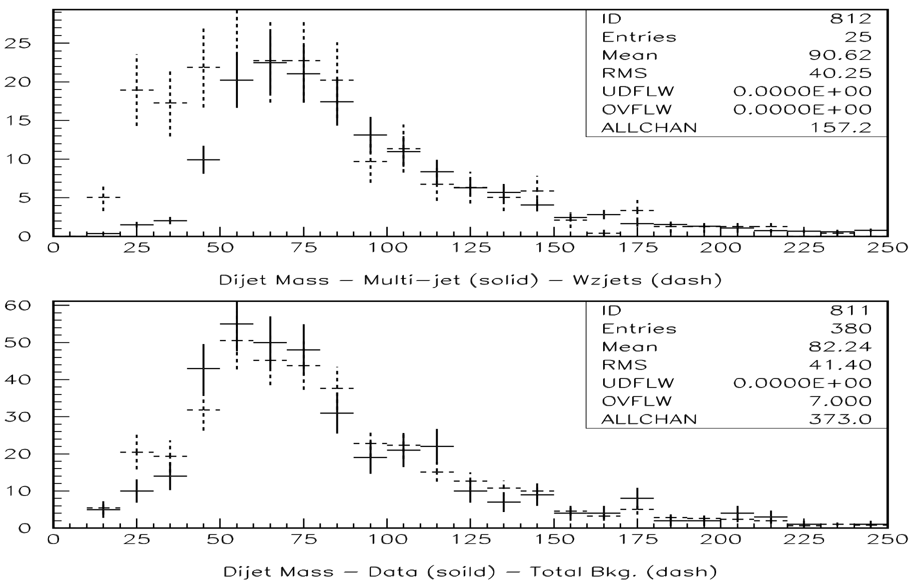

Figure 14: Comparison of data and background distributions: M(jj)

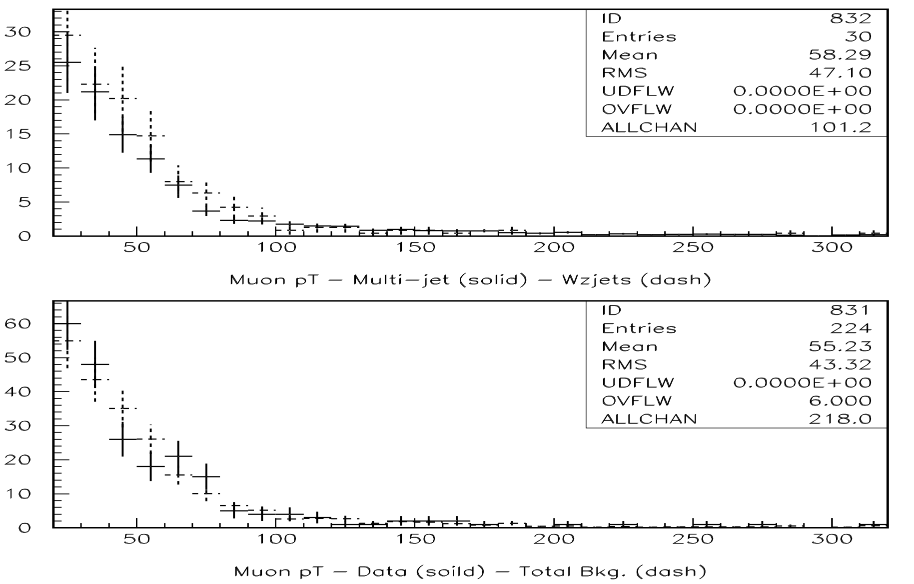

Figure 15: Comparison of data and background distributions: $p_T(\mu)$

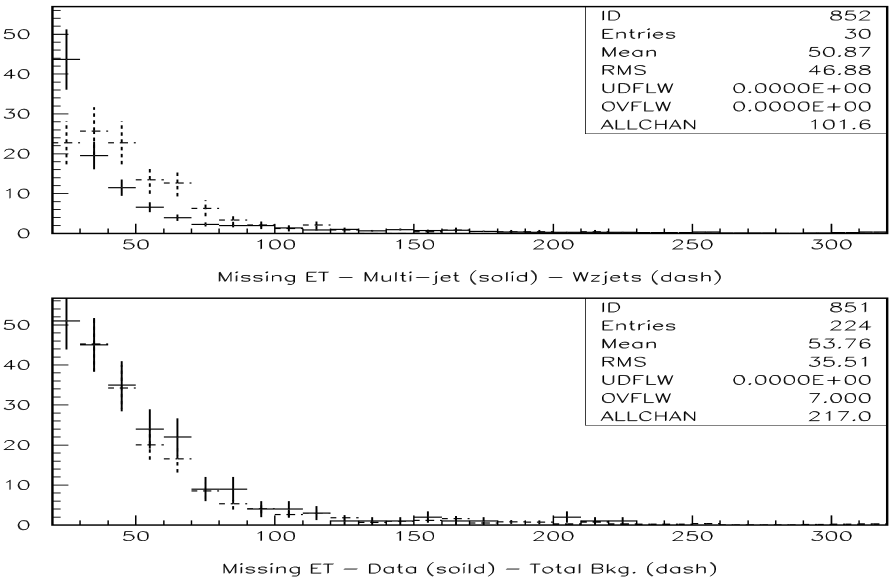

Figure 16: Comparison of data and background distributions: $\not{E}_T$

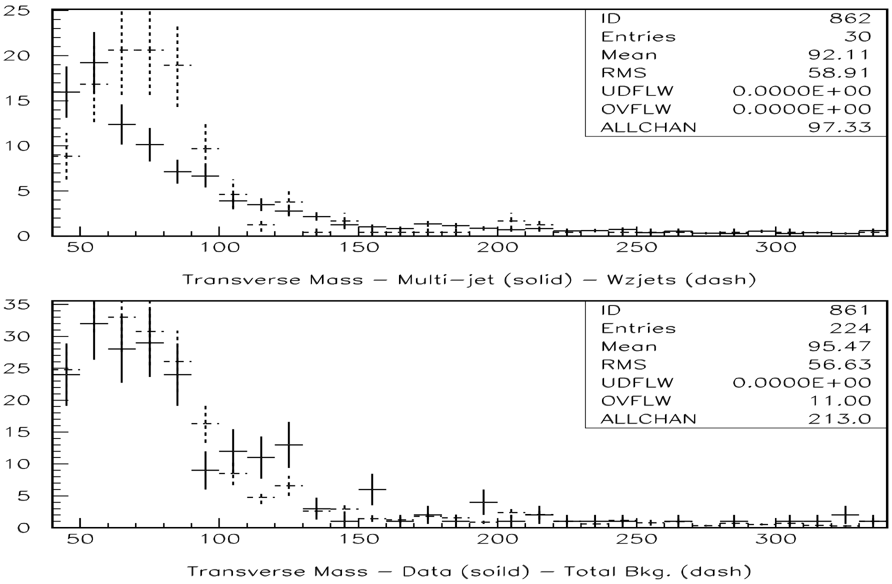

Figure 17: Comparison of data and background distributions: $M_T(\mu\nu)$

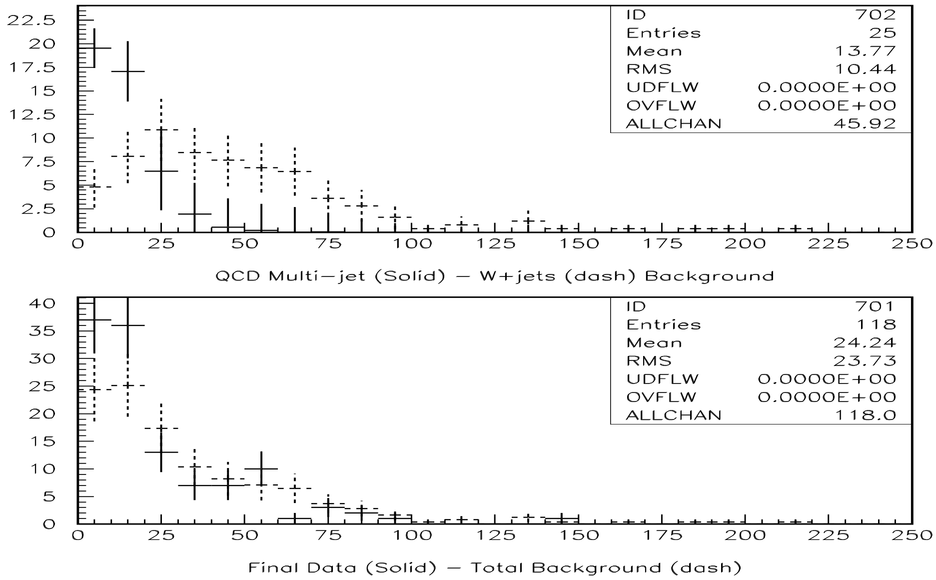

Figure 18: Comparison of data and background distributions: Standard cuts except for p_T(j) > 25 GeV/c.

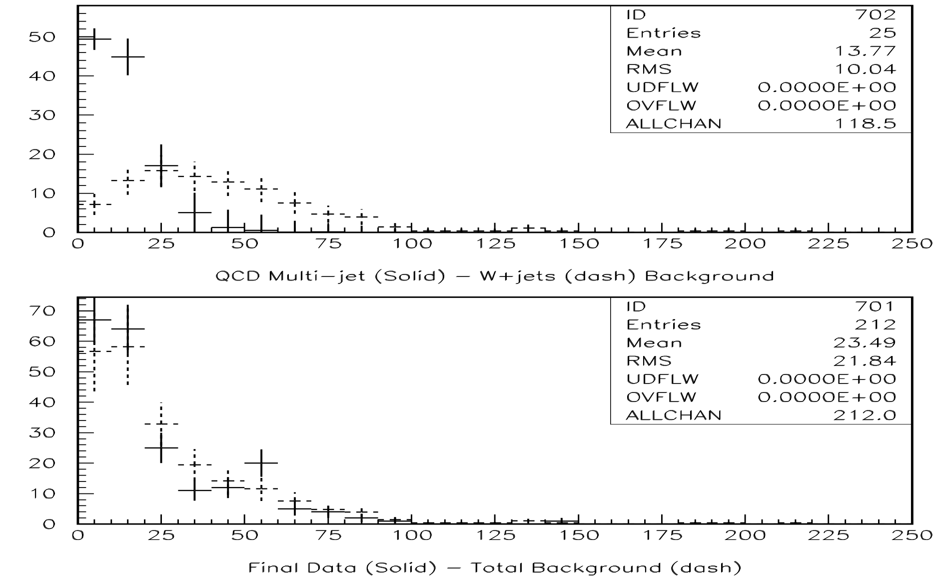

Figure 19: Comparison of data and background distributions: Standard cuts except for $M_T(\mu\nu)$ > 45 GeV/c.

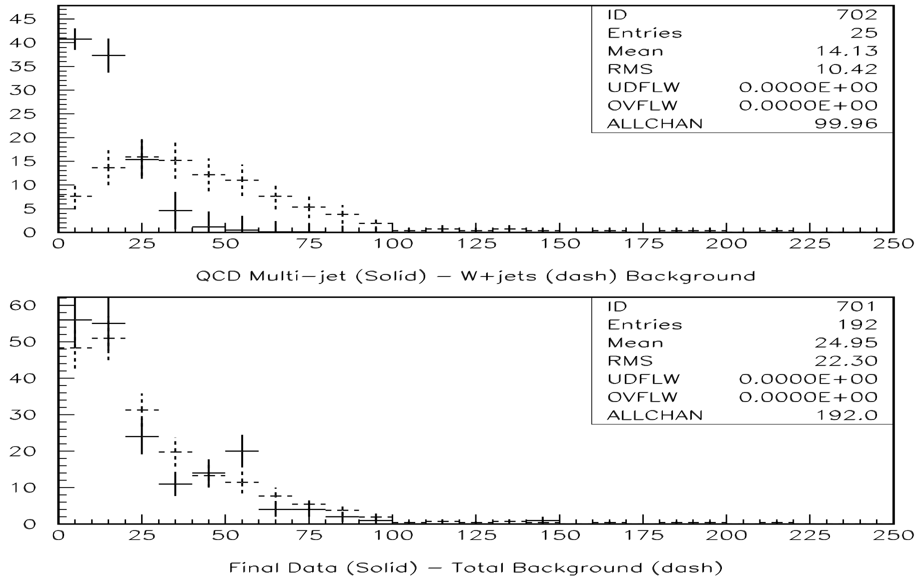

Figure 20: Comparison of data and background distributions: Standard cuts except for $\not{E}_T > 25$ GeV/c.

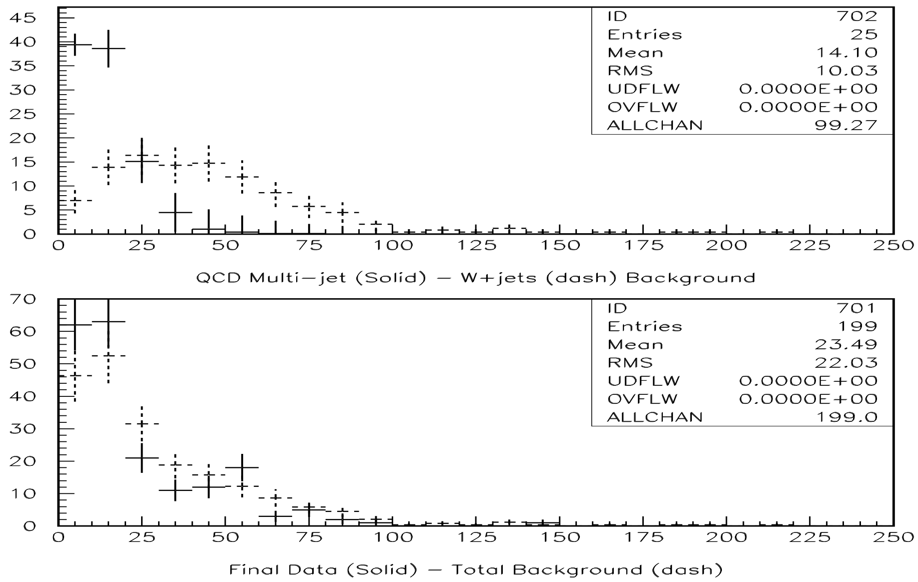

Figure 21: Comparison of data and background distributions: Standard cuts except for $p_T(\mu) > 25$ GeV/c.

Source of Error	Variation	Uncertainity
Missing $\not{E}_T$	± 5 GeV	7.2 %
Muon isolation δR	0.1	11.7 %
Jet energy scale	$\pm\sigma$	7.8 %
Dijet mass window	± 10 GeV	13.4 %
Transverse mass M_T	± 5 GeV	4.3 %
Total background - systematics	added in quadrature	20.4 %
Total background - statistical	added in quadrature	14.6 %
Total background uncertainity	added in quadrature	25.3 %

Table 10: Summary of background uncertainities for $WW/WZ \to \mu\nu jj$.

5 Fast Monte Carlo Simulation

We use a fast Monte Carlo event generator and fast detector simulation to model the effects of diboson production with anomalous couplings. The Generator-GEANT-Trigsim-Reco alternative would consume an impractical amount of computer resources due to the large number of Monte Carlo samples required (at each grid point in $\lambda-\Delta\kappa$ space).

WW and WZ production is modeled using a leading-order event generator [15]. This event generator has the capability to produce MC WW and WZ events with arbitrary values of the trilinear couplings. The output of the MC program is the production cross-section and a list of the four vectors of the boson decay products. Parton distribution functions are provided by PDFLIB[16]. We chose to use the MRSD-' distributions [17] with default input parameters. A k-factor of 1.335 is required. Next-to-leading order (NLO) simulations exist[18] but are not useful as event generators in this context.

The fast detector simulation is a streamlined version of DIPS [19]. In short, it models the acceptance and resolution of the DØ detector with parameterized resolutions. In order to simulate the kinematics associated with higher order processes, the WW system was boosted in the opposite direction to hadronic recoil according to the distribution provided by the Pythia[20] MC generator for SM WW production (the efficiency was 2.5% lower with no boost so we take half the difference as fractional systematic uncertainty). The event vertex is smeared by a Gaussian distribution with sigma of 30 cm. The muon fiducial acceptance is determined from a GEANT-Reco simulation[21] and is parameterized in an $\eta-\phi$ grid. The muon momentum resolution [22] is given by $\sigma(1/p) = 0.18(p-2)/p^2 \oplus 0.003$ (p in GeV/c). The jet energy resolution depends on the pseudorapidity of the jet and comes from a QCD group parameterization [23] determined using the dijet-balancing method. We used a look-up table to parameterize the jet acceptance as a function of $p_T(W)$ including the inefficiency from merging of the two jets from the W or Z boson decay and the dijet mass selection. This is described in more detail in subsection 5.1 below. The missing transverse energy was calculated from the vector sum of the E_T's of the smeared muon, the two smeared jets, and a contribution selected randomly from a distribution of the missing E_T in Minbias events collected in Run 1b. The efficiency of the jet part of the trigger came from the parameterization described in 3.1.1. The remainder of the muon reconstruction inefficiency and the muon trigger inefficiency, as discussed in sections 3.1.2 and 3.3 were applied as constant factors after the simulation program finished.

The output of the fast MC process was the cross section, the number of events generated, and a list of the $p_T(W)$ for the events that passed the simulation at a given grid point. We generated typically 10,000 events at each grid point. The 101 point grid used for the case $\Lambda = 1500$ GeV, $\Delta\kappa_\gamma = \Delta\kappa_Z$, $\lambda_\gamma = \lambda_Z$ is shown in Fig. 22.

5.1 Jet Acceptance in the Fast Monte Carlo

The jets from a W or Z decay at rest are back-to-back. If the bosons are boosted, the jets will be closer together. It is possible for the jets to overlap each other sufficiently that the jet algorithm reconstructs the two energies poorly. It is even possible that the jet algorithm cannot distinguish between the two jets, simply merging them into one. Therefore, the jet reconstruction efficiency depends on $p_T(W)$. The fast detector simulation does not account for this well on it's own. Therefore, we estimate this efficiency using Pythia Monte Carlo and the Geant simulation and then incorporate the results into the fast simulation.

We generated Standard Model events in 14 runs with $p_T(W)$ varying from 0 to 450 GeV/c. As $p_T(W)$ is a steeply falling spectrum we balanced the number of events at each $p_T(W)$ by applying an increasingly higher threshold in each run. Each run contained typically 2,500 events except for the the run with a threshold of 0 GeV which contained 4,999 events. These events were then processed through GEANT and reconstructed. Ntuples of the events were made using the same program as was used in the data processing.

We tabulated the jet efficiency in 10.0 GeV bins. First the muon p_T and fiducial cuts, the missing E_T cut, and the $\mu\nu$ transverse mass cut were applied, ensuring the kinematics of the events for which we're calculating the efficiency to match those of the fast simulation in which we will apply it. These events provide "the denominator". Next, we found the p_T of the boson which decayed to the jets using some information from the MC stored in the ntuple. For a few events this was ambiguous; we discarded them. We binned the events according to this (unsmeared) p_T. The efficiency is the number of events which passed the jet threshold criteria, the fiducial cuts and the dijet mass selection divided by the number of events in the denominator. Figure 23 displays the result.

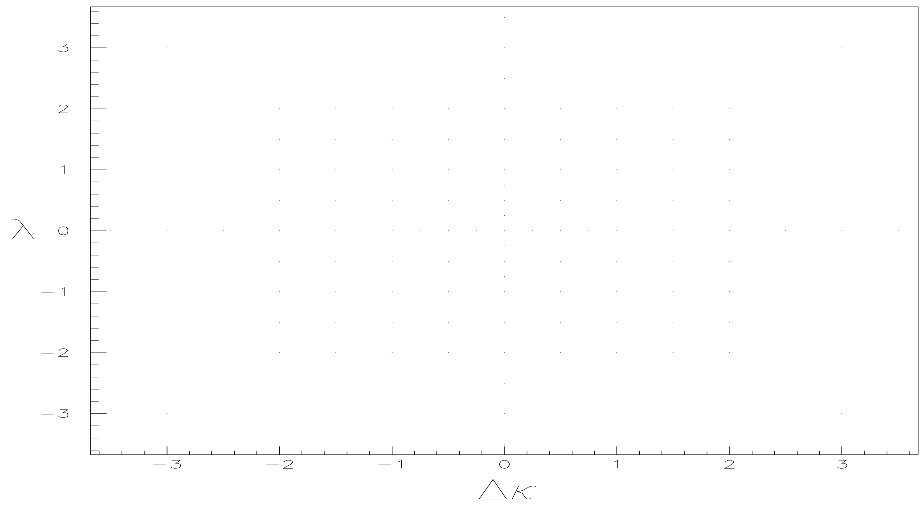

Figure 22: The grid of anomalous coupling parameters used in generating WW and WZ fast MC events.

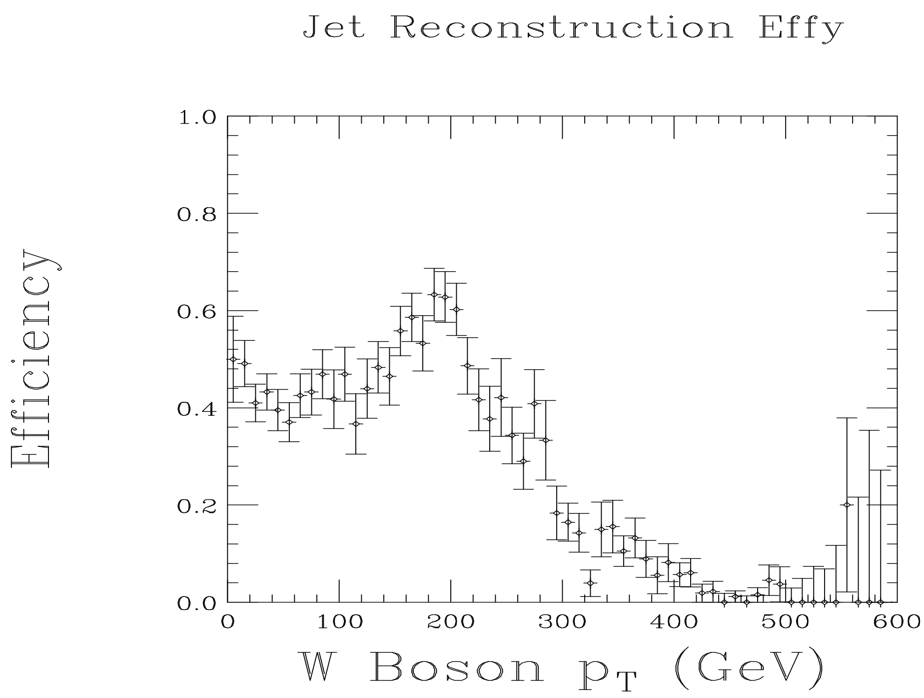

Figure 23: The efficiency of the jet selection as a function of $p_T(W)$ as calculated from the Pythia → Geant → Reco procedure. The p_T is unsmeared.

6 Standard Model Diboson Signal

We estimate the Standard Model prediction of the number of $WW(WZ) \rightarrow \mu\nu$jj events to be expected in the present data for an integrated luminosity of 80.7 pb^{-1}.

6.1 SM Cross Section Prediction

The WW production cross section is 10.1 pb^{-1} according to the Monte Carlo [15]. An uncertainty of 5% accounts for the variation in the cross section due to using different parton distribution functions or evolution scales [24]. The branching ratio to $\mu\nu$jj is [25] 0.104 ± 0.006 times 0.679 ± 0.015 times 2, for a total of 0.1412 ± 0.0086.

Similarly, the WZ production cross section is 2.6 pb^{-1} with a 5% uncertainty. The branching ratio for this decay mode is 0.104 ± 0.006 multiplied by 0.6990 ± 0.0015 [25], which is 0.0727 ± 0.0042.

6.2 Net Efficiency

The kinematic efficiencies for SM WW and WZ were studied with the fast MC simulation. A total of 1459 (1338) of 20,000 WW (WZ) events passed the kinematic and fiducial cuts. That's an efficiency of 0.073 ± 0.002 (0.067 ± 0.002).

The efficiency for SM WW events was slightly higher when calculated via the Pythia/GEANT/Reco route. We take half the difference as a systematic uncertainty in the overall efficiency. The efficiency of SM WZ events was about 1.5 σ higher when calculated via the Pythia/GEANT/Reco route. This is primarily due to applying a jet threshold efficiency based on $p_T(W)$ using the $W \rightarrow$ jj events for $Z \rightarrow$ jj. This difference would decrease for anomalous couplings because the effect of the threshold reduces. Again, we take half the difference as systematic uncertainty.

6.3 Calculation of the number of SM WW and WZ events

Table 11 summarizes the prediction for the number of events. We expect $4.04^{+0.54}_{-0.68}$ ($0.49^{+0.10}_{-0.11}$) $WW(WZ) \rightarrow \mu\nu$jj events. All of the uncertainties have been discussed previously. We take all the uncertainties as correlated except for the $W(Z) \rightarrow$ jj branching fractions, the statistical uncertainties in the kinematic and fiducial efficiencies, and most of the uncertainty in the WZ efficiency arising due to the difference between Pythia/Geant and the fast Monte Carlo (15% - 4.7% in quadrature). The sum is $4.53^{+0.59}_{-0.75}$ events.

Contribution/Channel	WW	WZ
Cross Section	10.1 ± 0.51	2.6 ± 0.13
Branching Fraction	0.1412 ± 0.0086	0.0727 ± 0.0042
Luminosity	80.7 ± 4.3 pb^{-1}	80.7 ± 4.3 pb^{-1}
Muon Trigger Eff'y	0.707 ± 0.018	0.707 ± 0.018
Muon ID Eff'y	$0.680^{+0.041}_{-0.080}$	$0.680^{+0.041}_{-0.080}$
Jet Trig and ID Uncert.	1 ± 0.038	1 ± 0.038
WW Boost Uncert.	1 ± 0.013	1 ± 0.013
Kin. & Fid. Cut Eff'y	0.073 ± 0.002	0.067 ± 0.002
Pythia/Geant vs. Fast MC	1 ± 0.047	1 ± 0.15
Number Predicted	$4.04^{+0.54}_{-0.68}$	$0.49^{+0.10}_{-0.11}$

Table 11: The prediction of the number of WW and WZ events given SM trilinear couplings. The sum of the two channels is $4.53^{+0.59}_{-0.75}$ events when correlated uncertainties are taken into account.

6.4 Final Data Sample Status

From the Table 11 and section 4, we collect the composition of the final data sample in Table 12. The SM predictions combined with estimated total background for the various processes account for all the events observed in the final data sample as indicated in Table 12.

Sample	Contribution	Total Uncertainity
Final data sample	224.0±15.0	6.7%
Total background	224.5±30.7	25.0%
SM Prediction	$4.5^{+0.6}_{-0.8}$	17.4%

Table 12: The contribution of various process to the final data sample with their total uncertainities for combined WW and WZ decays.

7 Anomalous Coupling Limits

From section 6, it is evident that we would observe excess events if anomalous gauge couplings were to be present. From Table 12, we conclude that the final data sample observed is consistent with SM predictions and the expected background. To quantify, we list the number of candidates and expected background events in all $p_T(W)$ region in Table 13.

$p_T(W)$ (GeV)	Candidates	Background	SM Predictions	Expected Events
$60 - 70$	5	8.9	0.9	9.8
$70 - 80$	5	6.4	1.5	7.9
$80 - 90$	2	4.6	1.1	5.6
$90 - 100$	1	2.1	0.5	2.6
$100 - 110$	0	0.4	0.3	0.7
$110 - 120$	0	0.8	0.2	1.0
> 120	1	3.7	0.2	3.9
> 150	0	1.7	0.1	1.8
> 170	0	1.3	0.0	1.3
> 200	0	0.4	0.0	1.0

Table 13: Comparison of observed candidates and expected total events as a function of high $p_T(W)$ region. The uncertainity in the background and prediction are 25% and 17.4% respectively. The observed events are consistent with SM predictions and expected background.

As there is no evidence of excess events signalling possible anomalous gauge couplings, we proceed to set limits on the anomalous coupling parameters λ and $\Delta\kappa$. This can be done using two different techniques: (i) the counting method and (ii) by fitting the entire $p_T(W)$ spectrum. Each method is separately discussed below.

7.1 Limits from the Counting Method

This method entirely relys on the fact that the events observed in the high $p_T(W)$ region is almost soley due to the anmalous couplings. Therefore counting the number of events after a cut off at a high $p_T(W)$, we can set an upper limit on the number of observed events at a given confidence level (CL) α. Limits on the anomalous coupling parameters can be extracted from the plane where:

$$N_{pred}(\lambda, \Delta\kappa) = N_{obs}(\alpha)$$

The contour defined by the the above equation is an ellipse in the $\lambda - \Delta\kappa$ plane which defines a finite area, the allowed deviation from the Standard Model values at a level α. As a consequence of low statistics, we use poisson probability for the the estimation of the upper limit $N_{obs}(\alpha)$. This method convolutes the $N_{obs}(\alpha)$ with a Gaussian distribution for uncertainities in luminosity, efficiencies and background [26].

$p_T(W)$ (GeV)	Candidates	Background	$\lambda_{\gamma=Z}$	$\Delta\kappa_{\gamma=Z}$
> 150	0	1.7	(-0.76, 0.78)	(-0.94 1.04)
> 170	0	1.3	(-0.78, 0.81)	(-0.98 1.07)
> 200	0	0.4	(-0.72, 0.78)	(-0.93 1.03)

Table 14: Limits from the counting technique for the anomalous gauge coupling parameters λ and $\Delta\kappa$ based on the assumption of same couplings for WWZ and $WW\gamma$ for $\Lambda_{FF} = 1.5$ TeV

Assuming equal couplings for WWZ and $WW\gamma$, we have listed the resulting limits on the coupling parameters for a number of $p_T(W)$ cuts in Table 14 for Λ_{FF}=1.5 TeV. These limits are obtained at 95% confidence level as axis limits, ie., the λ ($\Delta\kappa$) is constrained to be zero (SM value) while setting the limit on $\Delta\kappa$ (λ).

7.2 Limits from the Fitting of $p_T(W)$ Spectrum

The limits extracted using the counting method depends on the $p_T(W)$ cut and do not make use of the infomation available below the $p_T(W)$ cut in the spectrum. Moreover, these may also depend on normalization factors such as luminosity, efficiency and background corrections. Therefore, we could obtain more stringent limits by making a complete fit to the entire $p_T(W)$ or $p_T(jj)$ spectrum [27] as it uses all of information contained in the spectrum and is less sensitive to the overall normalization factors.

We use a binned maximum likelyhood technique to fit the $p_T(W)$ spectrum. The details of this technique are discussed elsewhere in great detail [28]. We choose 11 bins - 5 bins of 10 GeV starting at 0 and 5 bins of 20 GeV followed by a single bin of 350 GeV starting at 150 GeV. The last bin is usually chosen such that it is empty and is an important factor in setting the limits [29]. In this method, each bin can be considered as an independent and uncorrelated measurement. For jth bin, the probability P_j for observing N_J events is given by:

$$P_j = \frac{(b_j + L\epsilon\sigma_j(\lambda, \Delta\kappa))^{N_j}}{N_J!} e^{-(b_j + L\epsilon\sigma_j(\lambda, \Delta\kappa))}$$

where b_j is the background in that bin, L, the luminosity, ϵ the total reconstruction efficiency, and σ_j is the bin cross section. The product $\epsilon\sigma_j$ is extracted from the Monte Carlo. The the joint probability or the likelyhood for the distribution for a total of n bins is:

$$P = \prod_{j=1}^{n} P_j$$

As we normally measure L, b_j and ϵ with some uncertainity, we allow them to fluctuate around their nominal values with a Gaussian distribution of mean μ=1 and a root-mean-square deviation of the relevant uncertainity σ_μ:

$$P' = \int G_{f_n} df_n \int G_{f_n} df_n \sum_{j=1}^{n} \frac{(f_n n_j + f_b b_j)^{N_j}}{N_j!} e^{f_n n_j + f_b b_j}$$

with $n_j = L\epsilon\sigma_j$, the predicted number of events in jth bin. The above integrals are evaluated at 50 evenly spaced points between $\pm 3\sigma_\mu$. The set of couplings that best describe the data distribution is extracted at the point of maximum likelyhood in the $\lambda - \Delta\kappa$ plane. For convenience, we use the log-likelyhood, $L = logP'$ and the standard deviation errors are extracted along the contour $L_{max} - s^2/2$ [30]. At 95% CL, we obtain the 1-D limits and 2-D limits by setting s = 1.96, 2.45 respectively.

The log-likelyhood function obtained (for $\Lambda_{FF} = 1.5$ TeV) using the complete fitting of the $p_T(W)$ technique is shown in Figure 24. As expected, the maximum likelyhood is at the ($\lambda = 0$, $\Delta\kappa = 0$) bin. The final limits extracted along with the the bounds imposed by the unitarity condition are listed in Table 15. The relevant contour plots of 1-D limits are shown in Figures 25 and 26. For comparison, we have also listed the limits on the coupling parameters from $WW/WZ \to e\nu$jj [11] along with the muon channel limits in Table 16.

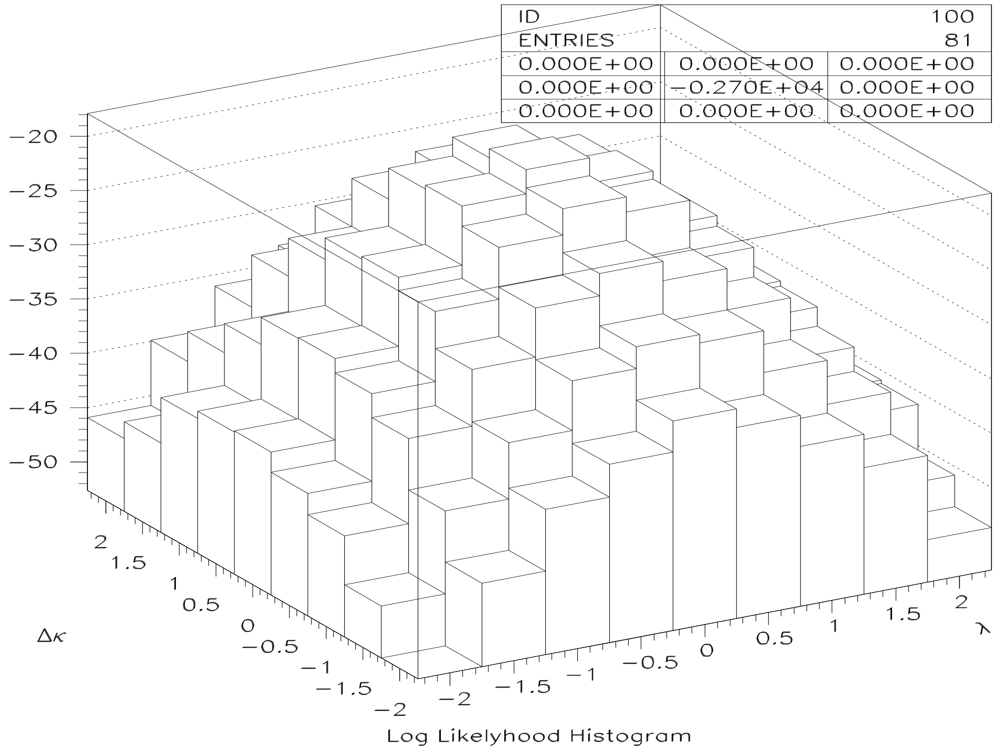

Figure 24: The log-likelyhood function L in $\lambda - \Delta\kappa$ plane for $\Lambda_{FF} = 1.5$ TeV. The L_{max} is at (0,0).

7.3 Limits for the HISZ Relations

So far, the anomalous gauge coupling parameters have been evaluated by assuming exactly same coupling for WWZ and $WW\gamma$. But in the literature, other forms of relations between WWZ and $WW\gamma$ couplings have been explored [31] and [32]. Here, we investigate one of them known as the HISZ relations [31]. These relations specify λ_Z, $\Delta\kappa_Z$, and g_{1Z} in terms of λ_γ and $\Delta\kappa_\gamma$:

$$\Delta\kappa_Z = \Delta\kappa_\gamma(1 - tan^2\theta_W)/2$$

$$\Delta g_{1Z} = \Delta\kappa_\gamma/2cos^2\theta_W$$

$$\lambda_Z = \lambda_\gamma$$

These relationships do preserve SU(2) X U(1) gauge invariance and is not well constrained by indirect measurements, suuch as the Z studies at LEP [33]. The corresponding 95% 1-D axis limits in the HISZ case are shown listed in Table 17. The

1-D 95% Confidence Level Axis Limits	Unitary Bounds	Λ_{FF} (in TeV)
$-0.45 < \lambda < 0.46$ ($\Delta\kappa$=0) $-0.62 < \Delta\kappa < 0.78$ (λ=0)	$\lvert\lambda\rvert < 0.82$ $\lvert\Delta\kappa\rvert < 1.17$	1.5
$-0.43 < \lambda < 0.44$ ($\Delta\kappa$=0) $-0.60 < \Delta\kappa < 0.74$ (λ=0)	$\lvert\lambda\rvert < 0.46$ $\lvert\Delta\kappa\rvert < 0.66$	2.0

Table 15: Limits from the $p_T(W)$ fit for the anomalous gauge coupling parameters λ and $\Delta\kappa$ based on the assumption of same couplings for WWZ and $WW\gamma$. For Λ_{FF} = 2.0 TeV, the unitary bounds are more stringent than the limits from the $WW/WZ \rightarrow \mu\mu$jj channel alone.

relevant contour plots in the HISZ case are displayed in Figures 27 and 28 along with the respective unitary bounds.

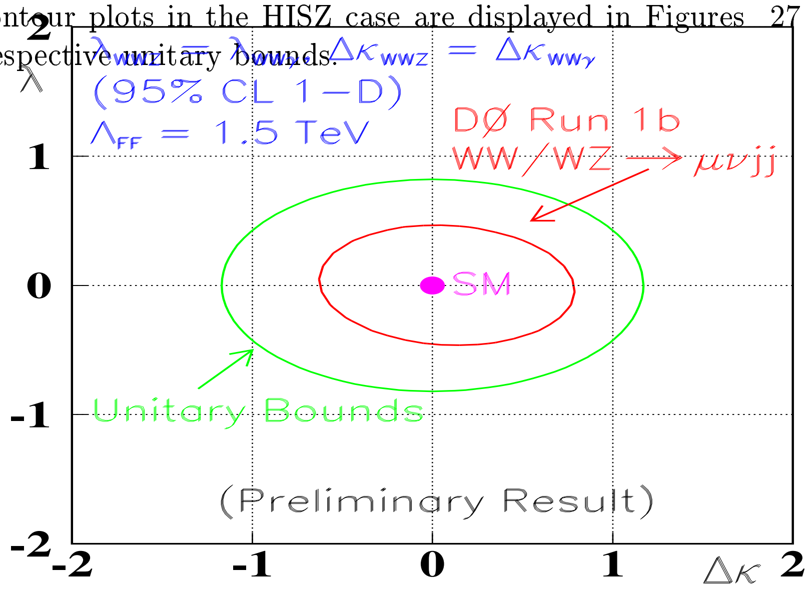

Figure 25: The contour diagram showing the limits for anomalous coupling parameters λ and $\Delta\kappa$ for Λ_{FF} = 1.5 TeV. The unitray bounds on λ and $\Delta\kappa$ are also shown.

Λ_{FF} (in TeV)	Channel	95% Confidence Level Axis Limits
1.5	$WW/WZ \to e\nu jj$	$-0.42 < \lambda < 0.44$ ($\Delta\kappa$=0)
		$-0.56 < \Delta\kappa < 0.75$ (λ=0)
	$WW/WZ \to \mu\nu jj$	$-0.45 < \lambda < 0.46$ ($\Delta\kappa$=0)
		$-0.62 < \Delta\kappa < 0.78$ (λ=0)
2.0	$WW/WZ \to e\nu jj$	$-0.38 < \lambda < 0.42$ ($\Delta\kappa$=0)
		$-0.52 < \Delta\kappa < 0.70$ (λ=0)
	$WW/WZ \to \mu\nu jj$	$-0.43 < \lambda < 0.44$ ($\Delta\kappa$=0)
		$-0.60 < \Delta\kappa < 0.74$ (λ=0)

Table 16: Comparison of anomalous coupling limits for channels $WW/WZ \to e\nu$jj and $WW/WZ \to \mu\nu$jj channels for $\Lambda_{FF} = 1.5$ and 2.0 TeV. The combined limits from the muon and electron channels will be more stringent than the unitary bounds even for $\Lambda_{FF} = 2.0$ TeV.

95% Confidence Level Axis Limits	Unitary Limits	Λ_{FF} (in TeV)
$-0.44 < \lambda < 0.46$ ($\Delta\kappa$=0)	$\lvert\lambda\rvert < 0.82$	1.5
$-0.75 < \Delta\kappa < 0.99$ (λ=0)	$\lvert\Delta\kappa\rvert < 2.17$	
$-0.42 < \lambda < 0.44$ ($\Delta\kappa$=0)	$\lvert\lambda\rvert < 0.46$	2.0
$-0.71 < \Delta\kappa < 0.96$ (λ=0)	$\lvert\Delta\kappa\rvert < 1.22$	

Table 17: Limits from the $p_T(W)$ spectrum fit for the anomalous gauge coupling parameters λ and $\Delta\kappa$ in the HISZ case for $\Lambda_{FF} = 1.5$ and 2.0 TeV. The unitary limits in this case are also shown in column 2.

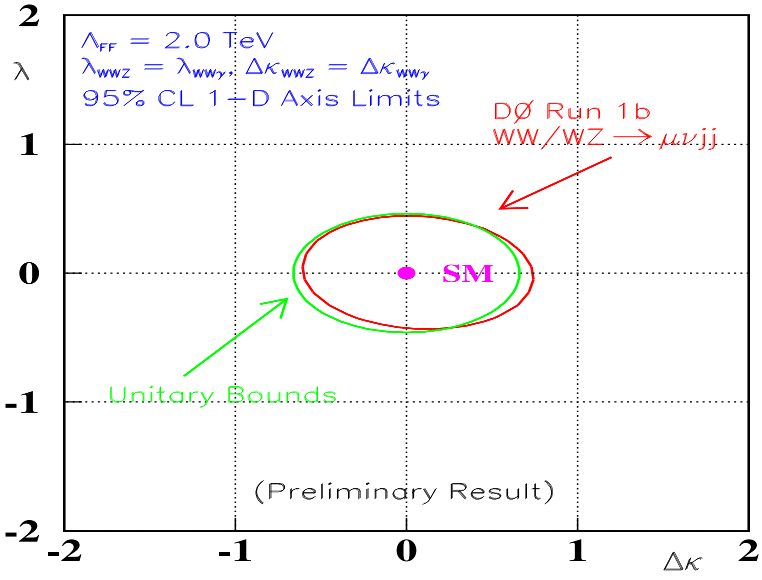

Figure 26: The contour diagram showing the limits for anomalous coupling parameters λ and $\Delta\kappa$ for $\Lambda_{FF} = 2.0$ TeV. The unitray bounds on λ and $\Delta\kappa$ are also shown.

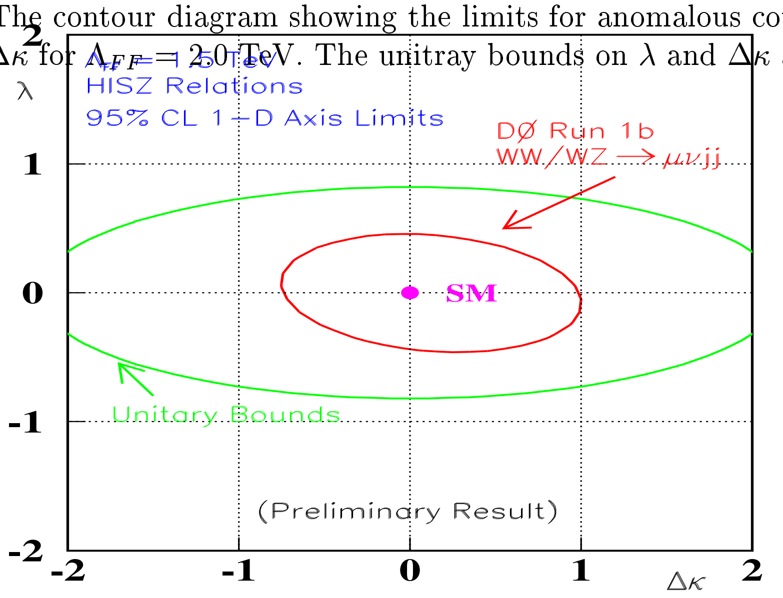

Figure 27: The contour diagram showing the limits for anomalous coupling parameters λ and $\Delta\kappa$ for $\Lambda_{FF} = 1.5$ TeV in HISZ case. The unitray bounds on λ and $\Delta\kappa$ are also shown.

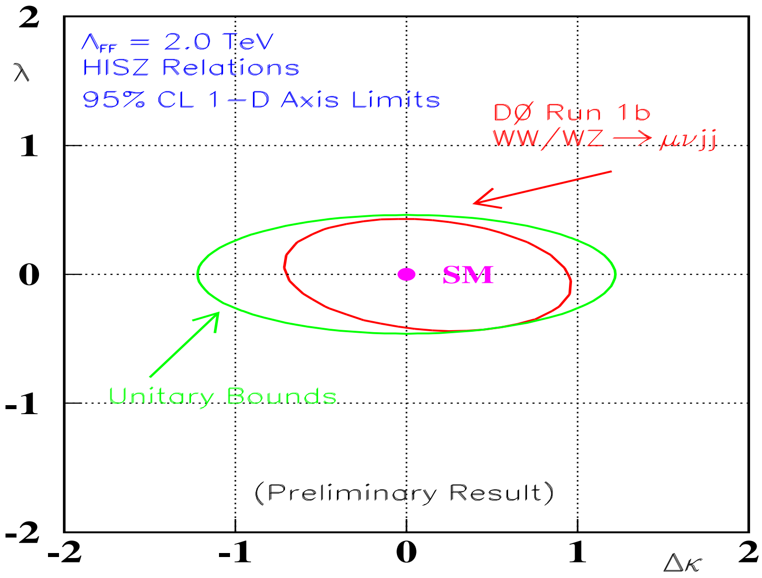

Figure 28: The contour diagram showing the limits for anomalous coupling parameters λ and $\Delta\kappa$ for $\Lambda_{FF} = 2.0$ TeV in the HISZ case. The unitray bounds on λ and $\Delta\kappa$ are also shown.

8 Conclusion

Using DØ Run 1b data with an integrated luminosity of 80.7 pb^{-1}, we have searched for the presence of anomalous gauge couplings in the channel $WW/WZ \rightarrow \mu\nu jj$. The final results indicate no evidence of such anomalous couplings as the $p_T(W)$ spectrum is in accordance with the predictions of the Standard Model and expected background for this process. Therefore, we are able to set limits on the anomalous coupling parameters λ and $\Delta\kappa$. The 1-D and 2-D 95% CL axis limits obtained by a complete fit of the $p_T(W \rightarrow \mu\nu)$ spectrum are summarized in the table below.

Type	1-D Limits		2-D Limits	
	λ ($\Delta\kappa$=0)	$\Delta\kappa$ (λ=0)	λ ($\Delta\kappa$=0)	$\Delta\kappa$ (λ=0)
"$WWZ = WW\gamma''$ $\Lambda_{FF} = 1.5$ TeV UL: $\|\lambda\| < 0.82$, $\|\Delta\kappa\| < 1.17$	(-0.45 0.46)	(-0.62 0.78)	(-0.57 0.58)	(-0.80 0.96)
"$WWZ = WW\gamma''$ $\Lambda_{FF} = 2.0$ TeV UL: $\|\lambda\| < 0.46$, $\|\Delta\kappa\| < 0.66$	(-0.43 0.44)	(-0.60 0.74)	(-0.54 0.55)	(-0.77 0.90)
"HISZ Relations" $\Lambda_{FF} = 1.5$ TeV UL: $\|\lambda\| < 0.82$, $\|\Delta\kappa\| < 2.17$	(-0.44 0.46)	(-0.75 .99)	(-0.56 0.57)	(-0.96 1.21)
"HISZ Relations" $\Lambda_{FF} = 2.0$ TeV UL: $\|\lambda\| < 0.46$, $\|\Delta\kappa\| < 1.22$	(-0.42 0.44)	(-0.71 0.96)	(-0.53 0.54)	(-0.92 1.16)

Table 18: Summary of anomalous coupling axis limits at 95% CL in the channel $WW/WZ \rightarrow \mu\nu$jj. Here "UL" stands for unitary limits - the bounds imposed by the unitary condition on the coupling parameters. The symbol "$WWZ = WW\gamma$" denotes the assumption of same couplings for WWZ and $WW\gamma$, i.e, $\lambda_Z = \lambda_\gamma$ and $\Delta\kappa_Z = \Delta\kappa_\gamma$.

The limits shown above are comparable to those obtained in the channel $WW/WZ \rightarrow e\nu$jj [28]. Adding the muon and the electron channels together as $WW/WZ \rightarrow l\nu$jj, the combined limits will be certainly more stringent for the anomalous coupling parameters λ and $\Delta\kappa$.

9 Acknowledgements

We received help from many sources to complete this analysis project. We are particularly grateful to Steve Wimpenny, Taka Yasuda, Alberto Sanchez and the members of the Diboson Group for many useful and enlightening discussions. This analysis would not have been possible without help from John Hobbs and the Top Group, who provided the data sample and the procedure for estimating the background. Nobu Oshima deserves thanks and credit for generating the Pythia diboson samples used in this analysis.

References

[1] K. Hagiwara, R. D. Peccei, D. Zeppenfeld, and K. Hikasa, Nucl. Phys. **B282**, 253 (1987).

[2] K. Gaemers and G. Gounaris, *Z. Phys. C1*, 259 (1979).

[3] Much detailed documentation regarding the data, Monte Carlo samples, etc ... can be found in the area http://www-d0.fnal.gov/physics_analysis/top/mujets.

[4] Tom Rockwell, private communication.

[5] P. Quintas, "Trigger Efficiency for $W \to \mu\nu$ in Run 1B", DØNote 2712 (September 1995).

[6] J. Hobbs, private communication. See the top group documentation located at URL: http://d0wop.fnal.gov/ cobau/d0_private/muon_efficiency_study.html.

[7] P. Quintas, "Reconstruction and Selection Efficiencies for High p_T Muons in Run 1B", DØNote 2865 (February 1996).

[8] D. Hedin, T. Lagger, and C. Nicholson, "Run 1B Muon Event Scanning", DØNote 2716 (September 1995).

[9] M. Bhattacharjee, V. D. Elvira, G. Blazey, "Efficiencies of Standard Jet Cuts for Cone Sizes: 0.3, 0.5, 0.5", DØNote 2197 (July 1994).

[10] A. L. Lyon, "A Search for Squarks and Gluinos Using the Jets and Missing Energy Signature at DØ", Ph. D thesis, U. of Maryland, 1997, (unpublished).

[11] A. Sanchez-Hernandez, "Experimental bounds on $WW, WZ \to e\nu$jj production at DØ", DØNote 3129 (November 1996).

[12] J. M. Butler *et al.*, "Measurement of the Top quark production cross section using *lepton* + jets events", DØNote 2978 (December 1995).

[13] B. Abbot *et al.*, DØ Collaboration, "Measurement of the Top Quark Pair Production Cross Section in $p\overline{p}$ Collisions", Submitted to the XVIII International Symposium on Lepton-Photn Interactions, July 28 - August 1, 1997, Hamburg, Germany, FERMILAB-Pub-97/109-E.

[14] S. Abachi *et al.*, DØ Collaboration, "Top Quark Search with the DØ 1992-1993 Data Sample", Phys. Rev. **D52**, 4877 (1995), FERMILAB-PUB-95/130-E.

[15] K. Hagiwara, J. Woodside, and D. Zeppenfeld, Phys. Rev. D **41**, 2113 (1990).

[16] "PDFLIB User's Manual Version 5.02", H. Plothow-Besch, CERN-PPE W5051 (1994).

[17] A.D. Martin, R.G. Roberts and W.J. Stirling, Phys. Rev. D **47**, 867 (1993).

[18] J. Ohnemus, Phys. Rev. D **44**, 1403 (1991); U. Baur, T. Han, and J. Ohnemus, HEP-PH-9410266 (1994); J. Ohnemus, *Proceedings of the International Symposium on Vector Boson Self-Interactions*, Los Angeles, CA, 1995, edited by U. Baur, S. Errede, and T. Muller, p. 60.

[19] S. Glenn, "A parametric detector simulation for dibosons", DØNote 2846 (January 1996). This program has been used in several published diboson analyses.

[20] "Pythia 5.6 and Jetset 7.3 Physics and Manual", T. Sjöstrand, CERN- TH-6488/92 (1992).

[21] "Measurement of $Z\gamma \to \mu\mu\gamma$ and Limits on Trilinear $ZZ\gamma$ and $Z\gamma\gamma$ Couplings", M. Adams *et al.*, DØNote 3230 (May 1997). The efficiency table for the "loose muon selection" of the $Z\gamma$ analysis has the same $\eta - \phi$ dependence as this analysis and is used here.

[22] "Muon Momentum Determination", C. Gerber *et al.*, DØNote 2140, (Oct. 1994).

[23] "Jet Energy Resolution", M. Bhattacharjee, G. Blazey, and R. Hirosky, DØNote 2557 (1995).

[24] "Search for W Boson Pair Production with Dilepton Decay Modes with Run 1B Data", P. Bloom, H. T. Diehl, and T. Yasuda, DØNote 3290, (August 1997).

[25] The Particle Data Group, R. M. Barnett *et al.*, Phys. Rev. D **54**, 1 (1996).

[26] R. Partridge, "Top Limit Calculation", DØ Note 1806 (1993).

[27] B. P. Roe, "Probability and Statistics in Experimental Physics", Springer Verlag, New York 91992).

[28] A. Sánchez-Hernández, "Search for Anomalous $WW/WZ \to e\nu jj$ Production at DØ", Ph. D Dissertation, Centro de Investigación y de Estudios Avanzados, Mexico City, Mexico (1997). Also see references therein.

[29] G. Landsberg, in proceedings of Workshop on Physics at current accelerators and the Supercollider, ANL-HEP-CP-93-92, 303 (1992); Also "Test of the Standard Model of Electroweak Interactions by Measuring the Anomalous $ZZ\gamma$ and $Z\gamma\gamma$ Couplings", Ph. D Dissertation, SUNY at Stony Brook (1994).

[30] R. M. Barnett *et al.*, (The Particle Data Group), Phys. Rev. **D54**, 201, 210 (1996).

[31] K. Hagiwara, *et al.*, Phys. Rev. **D48**, 2182 (1993).

[32] P. Hernandez, "Triple Gauge Couplings: Does LEP-1 obviate LEP-2?", Proceedings of the International Conference on Vector Boson Self-Interactions, ed. by U. Baur, *et al.*, AIP (1995).

[33] D. Schaile, "Precision Data from LEP", Proceedings of the International Conference on Vector Boson Self-Interactions, ed. by U. Baur, *et al.*, AIP (1995).